A STUDY ON COBALT SUBSTITUTED SnSb NANO ALLOY

By

P.Aarthi

(11PHS01)

A dissertation submitted to

AVINASHILINGAM INSTITUTE FOR HOME SCIENCE AND HIGHER EDUCATION FOR WOMEN,

COIMBATORE - 641 043.

In partial fulfilment of the requirements for the degree of

MASTER OF SCIENCE IN PHYSICS

MAY 2013

A STUDY ON COBALT SUBSTITUTED SnSb NANO ALLOY

By

P.Aarthi

(11PHS01)

A dissertation submitted to

AVINASHILINGAM INSTITUTE FOR HOME SCIENCE AND HIGHER EDUCATION FOR WOMEN,

COIMBATORE -641 043.

In partial fulfilment of the requirements for the degree of

MASTER OF SCIENCE IN PHYSICS

MAY 2013

Certified as a Bonafide Research Work

Rachel 10.5.13

Signature of the Head of the Department

B. Vale 09/05/13

Signature of the Guide

ACKNOWLEDGEMENT

I owe my sincere thanks to **Lord Almighty and My Lovable Parents** without Whom I Would has been nothing and showering their generous blessings upon me in all endeavors.

I am grateful to **(Thiru.) T.S.K. Meenakshisundaram,** M.A., M.Phil., PhD. Chancellor, Avinashilingam Institute for Home Science and Higher Education for Women, Coimbatore, for providing the opportunity to conduct this study.

My Sincere thanks to **Hon. Colonel. Dr. (Tmt.) Sheela Ramachandran,** M.Sc., P.G. Dip., PhD. (Avinashilingam), Vice Chancellor, Avinashilingam Institute for Home Science and Higher Education for Women, Coimbatore, for providing all the necessary facilities for the study.

I express my humble thanks to our former Vice Chancellor, **Hon. Colonel. Dr. (Tmt.) Saroja Prabhakaran,** M.A., Dip. Ed., (Madras), Ph.D. (Mother Teresa), of Avinashilingam Institute for Home Science and Higher Education for Women, Coimbatore, for the moral support, Kind blessing and for providing the adequate help required to carry out the study.

My hearty thanks to **Dr. (Tmt.) Gowri Ramakrishnan,** M.Sc., (Madras), M.Phil., Ph.D. (Avinashilingam), Registrar, Avinashilingam Institute for Home Science and Higher Education for Women, Coimbatore, for providing adequate facilities required to carry out the work.

My thanks to **Dr. (Tmt.) R. Parvatham,** M.Sc., Dip.Ed, M.Phil., (Madras), Ph.D. (Avinashilingam), Dean, Faculty of Science, Avinashilingam Institute for Home Science and Higher Education for Women, Coimbatore, for her support in the completion of my thesis.

I whole heartily thank **Dr. (Tmt.) Rachel Oommen,** M.Sc. (Kerala), Dip.Ed. (Madras), B.Ed. (Annamalai), M.Phil., Ph.D. (Bharathiar), Professor and Head of the Department of Physics, Avinashilingam Institute for Home Science and Higher Education for Women, Coimbatore, for her encouragement and generous help which was of great value.

I express my heartiest thanks to my guide **Dr. (Tmt.) B.Nalini,** M.Sc., Ph.D., M.S (Edu.Mgt.), STA Fellow, AIST Fellow (Japan), Assistant Professor, Department of Physics, Avinashilingam Institute for Home Science and Higher Education for Women, Coimbatore, for her inspiring guidance, meticulous care, patience, help, encouragement, motivation, and skillful and expert suggestions in completion of this work.

I also wish to thank **all the staff members** of the Department of Physics, Avinashilingam Institute for Home Science and Higher Education for Women, Coimbatore, for their help and encouragement.

I would like to express my special thanks to **my dear friends and all my well wishers** for their constant encouragement, support and help in carrying out this work successfully.

AARTHI.P

CONTENTS

CHAPTER III Page No

SYNTHESIS AND EXPERIMENTAL TECHNIQUES

CHAPTER IV Page No

RESULTS AND DISCUSSION

CHAPTER V Page No

SUMMARY AND CONCLUSION

List of Figures

List of Table

CHAPTER –I
INTRODUCTION

1.1 Introduction

A lithium ion battery is a rechargeable battery type. It is one of the most popular batteries high energy density (because of lithium ion batteries are high voltage), no memory effect, durability, cost, and especially with regards to safety, lightest weight, low maintenance and slow loss of charge. It is widely used as power supplies for portable electronic devices such as cellular phones, digital cameras, smart phones and notebook PCs [1]. It is also applied in electric vehicle and aerospace. In 1989, it was cathode containing polyanions, then 1991, the first commercial lithium ion battery was released. In 2002, there is an improvement in the conductivity of lithium ion battery. In 2004, again there is an increasing performance, but 2011, lithium ion batteries account for 66% of all portable secondary rechargeable battery.

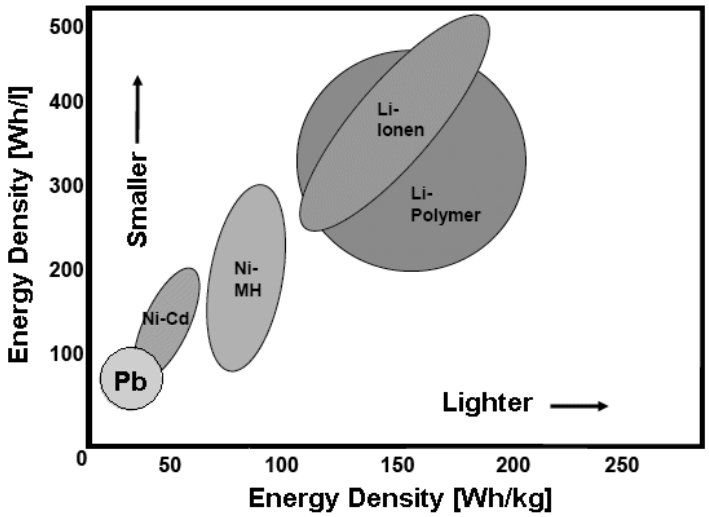

Figure 1.1 Energy storage Rechargeable battery systems

The specific energy density per unit weight (150-250 (W.h/kg) and the specific power density per unit weight (300-1500 W/kg) [2]. The volumetric energy density per unit volume (250-620 W.h/l) [3]. It is produce the 3.6 volts, approximately three times the voltage of rechargeable nickel cadmium batteries. Lithium ion does not need to be fully charged; a partial charge is better.

1.2 Overview of Lithium Ion Battery

A Lithium ion battery is an electrochemical device that is converted the chemical energy. Mainly, Lithium-ion batteries are used for the anodes due to their high safety, good electrical conductivity and high capacity [4]. Anode, Cathode, Separator and Electrolytes are part of batteries. Both the anode and cathode are materials into which and from which lithium can migrate. The process of lithium moving into the anode or cathode is referred to as insertion (or intercalation) and the reverse process, in which lithium moves out of the anode or cathode, is referred to as extraction (or deintercalation).

Reactions of Lithium ion battery:

- Positive Electrode

Charge

$$LiCoO_2 \leftrightarrows Li_{1-x}CoO_2 + xLi + xe^-$$

Discharge

- Negative Electrode

Charge

$$Cy + xLi + xe^- \leftrightarrows CyLi_x$$

Discharge

- Overall

Charge

$$LiCoO_2 \leftrightarrows Li_{1-x}CoO_2 + CyLi_x$$

Discharge

1.2.1 Anode Materials

Anode is the electrode where always oxidation takes place. The anode (or negative electrode) in lithium ion battery is typically made up of Graphite, coated on Copper foil. Due to its electronic structure, it is highly conductive and can reach 25000 S/cm^2 in the phase of a single crystal. This unique particle structure realizes superb performance and high capacity. The lithium ion batteries are targeting in higher specific capacity. In lithium ion batteries, lithium compounds are used as anode.

Features of Anode Material

- Maximize the usage time of lithium ion batteries through its high capacity.
- Maintaining the prime performance at low temperature.
- High output
- High safety
- High voltage
- High durability
- Cyclic stability
- High rate capability

1.2.2 Cathode Materials

A cathode is the electrode of an electrochemical cell at which reduction occurs. The cathode (or positive electrode) in lithium ion battery made with lithium cobalt oxide has a current collector made of thin aluminium foil. In lithium cobalt oxide average voltage is 3.7V and gravimetric capacity is 140 mA.h/g. In cobalt the nominal voltage of cathode material is 3.60V, the charge limit is 4.20V, the charge and discharge rates are 1C limit and the energy density 110-190 (W.h/kg).

Features of Cathode Material

- High discharge current
- High lithium capacity
- Low temperature capacity retention
- Poor conductivity
- Excellent high rate capacity
- Low degradation
- Cycle stability
- Good ion mobility

1.2.3 Electrolytes

An electrolyte made with lithium salt in an organic solvent. There are two types of electrolytes such as solid electrolyte and liquid electrolyte. The solvent is mixtures of organic carbonates such as dimethyl carbonate (DMC) and ethylene carbonate (EC). The salt is such as lithium hexafluoro phosphate. Solid electrolytes are stable, reliable easy to prepare and can change it in any shape for making in different battery. A solid electrolytes enables the lithium metal to cycle well, with highly enhanced safety and the conductivity range is 10^{-3} S/cm < σ < 10 S/cm.

- Ion conductor between cathode and anode
- Solid electrolyte is also possible if the ion conductivity is high at operating temperature.
- Requirement inert
- High ionic conductivity, low viscosity
- Low melting point
- Appropriate concentration of lithium salt
- Chemical/thermal stability
- Low cost
- Environmental friendly, non toxic.

1.3 Principle of Lithium Ion Battery

A lithium-ion battery is a type of rechargeable battery made of lithium metal. Lithium ions move from the negative electrode to the positive electrode during discharge and back during charging. Lithium is a very light metal with high chemical potential, hence used in making batteries for light portable consumer electronics such as mobile phones and laptops.

Lithium-ion battery anode is carbon materials such as graphite. Cathode is the transition of lithium metal oxides, such as $LiMn_2O_4$. Containing lithium salt electrolyte is the organic solution. Lithium-ion batteries are usually non-Lithium. Charging, driven by the electric field of lithium-ion lattice emerge from the cathode, the electrolyte to the anode embedded in the crystal lattice. Discharge, the opposite process, lithium-ion to return to cathode, through the use of electronic appliances from the circuit and reach the cathode of lithium-ion. As lithium-ion battery does not contain any precious metals and raw materials are cheaper, much room for price cuts should be the most expensive batteries. At present the media frequently reported solid polymer lithium batteries or lithium batteries, in fact its main components: cathode, the anode and the electrolyte and are working principle and use of the liquid electrolyte lithium-ion battery, only divide and different packaging materials, it is still a lithium-ion batteries. And compared to the traditional secondary batteries, lithium-ion batteries have outstanding advantages: high-voltage lithium-ion battery voltage in the 3.6 V is the nickel-cadmium and nickel-hydrogen battery voltage three times. In many small electronic products, a battery can be used to meet demand. This is also with other major difference between the secondary batteries, can only be used for lithium-ion battery charger to recharge, so as to avoid accidents. The high-energy lithium-ion battery than the current energy has reached 140 Wh/kg, is the nickel-cadmium battery three times, nickel-hydrogen batteries of 1.5 times. The current cycle of long life cycle life lithium-ion battery has reached more than 1000, in the discharge depth of up to the low tens of thousands of times over several other secondary batteries. Since the discharge of small lithium-ion battery self-discharge rate of 6-8 percent, far lower than the nickel-cadmium batteries (25 to 30 percent) and nickel-metal hydride batteries (30 to 40 per cent). No memory effect can be requested at any time to recharge, and not reduce battery performance. On the environment pollution-free lithium-ion battery does not exist in harmful substances, is truly "green batteries"

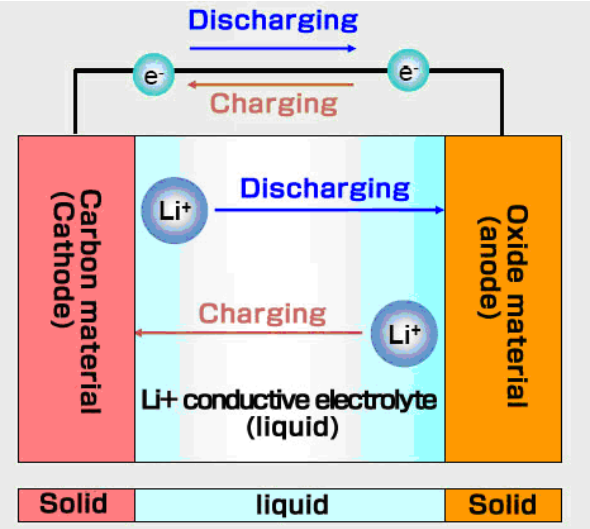

Figure 1.2 Schematic representation of Operating Principle of Lithium ion battery

1.4 General Considerations of Lithium ion Battery

1.4.1 Charge and Discharge

Li-ion batteries, like other batteries, are constructed from three primary materials: two electrodes (anode and cathode) and a conductive electrolyte. In the case of Li-ion batteries monovalent lithium cations migrate to the negative electrode (anode) during charging cycles and to the positive electrode (cathode) during discharge cycles. Monovalent lithium cations migrate to the negative electrode (anode) during charging cycles and to the positive electrode (cathode) during discharge cycles [5, 6].

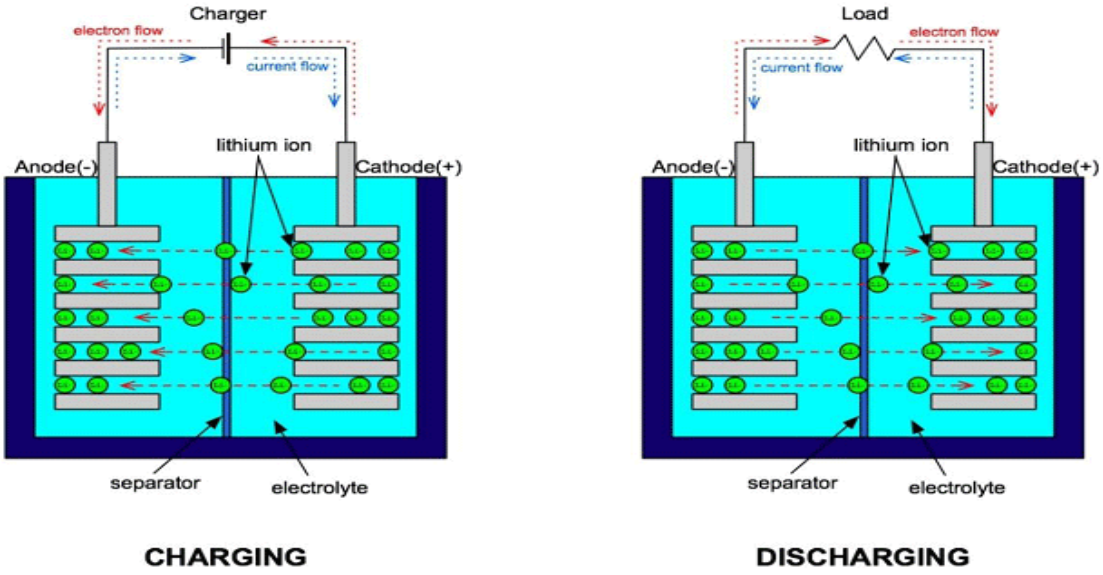

Figure 1.3 Schematic representation of Charging (left) and Discharging (right) of Lithium ion battery

During charging, the positive active material is oxidized, producing electrons, and the negative material is reduced, consuming electrons. During discharge Lithium ions are dissociated from the anode and migrate across the electrolyte and are inserted into the crystal structure of the host compound. At the same time the compensating electrons travel in the external circuit and are accepted by the host to balance the reaction. The process is completely reversible. Thus the Lithium ions pass back and forth between the electrodes during charging and discharging.

1.5 Objectives

- Preparation of Tin-Antimony in Stable Phase.
- Preparation of Sn_xSb_y metal alloy powders at different ratios and characterizing structural and compositional analysis.

1.6 References:

1. Sukeun Yoon, Jae-Myung Lee, Hansu Kim, Dongmin Im, Seok-Gwang Doo, Hun-Joon Sohn; An Sn–Fe/carbon nanocomposite as an alternative anode material for rechargeable lithium batteries; Electrochimica Acta; 54(10); 2699-2705; 2009.
2. Rechargeable lithium ion battery OEM Battery products; Panasonic.com; 23 April 2010.
3. Application of silicon based Alloy in anode; greencarcongress.com; 31 Jan 2011.
4. Kai Zhuo, Myung-Gi Jeong, Chan-Hwa Chung, Suwon ; Highly porous dendritic Ni–Sn anodes for lithium-ion batteries; Journal of Power Sources; 440-746;2013.
5. Manthiram, A. Materials Aspects: An Overview. In Lithium Batteries: Science and Technology; Nazri, G.-A. and Pistoia, G., Eds.; Springer: New York, 2003.
6. Yoshio, M. and Noguchi, H. A Review of Positive Electrode Materials for Lithium-Ion Batteries; In Lithium-ion Batteries: Science and Technology; Yoshio, M; Brodd, R.J.; Kozawa, A., Eds.; Springer: New York, 2009.

CHAPTER –II
REVIEW AND LITERATURE

2.1 Review of Literature

1. **Schmidt P.C *et al.,* (1992)** studied the electronic band structure, the density of states, and the electronic charge density distribution of K [SnAs], K [SnSb], and Sr [Sn_2 As_2] by means of self-consistent density-functional calculations in the local approximation. The valence bands and the conduction bands are separated by a band gap which in one case (Sr [Sn_2As_2]) is nearly zero. The fully occupied valence bands can be identified as s- and p-like bands of Sn, As, and Sb. These results indicate that the alkali and alkaline earth atoms form a cationic substructure. The Sn and As/Sb atoms form covalent and negatively charged layer structures. The correlations between the Zintl concept and the calculated band structures are discussed.
2. **Robert Lam *et al.,* (2000)** has been synthesized the ternary Zintl compound europium tin antimonide, $EuSn_3Sb_4$, at 900ºC in the presence of a tin flux, and its structure has been determined by single-crystal X-ray diffraction methods. It crystallizes in the orthorhombic space group D^{16}_{2h}-Pnma with a=9.954(2), b=4.3516(7), c=22.650(4) Å, and Z=4 at 223C. $EuSn_3Sb_4$ is isostructural to $SrSn_3Sb_4$; it possesses channels defined by an anionic framework of shared $SnSb_4$ tetrahedra, $SnSb_3$ trigonal pyramids, and Sb-Sb zigzag chains, and it is filled by Eu^{2+} cations. Resistivity measurements indicate weakly metallic behavior for ASn_3Sb_4 (A=Eu, Sr) and the structurally related $Ba_2Sn_3Sb_6$. The anisotropic metallic nature of these compounds is explained through extended Huckel band structure calculations.
3. **Musikhin S *et al.,* (2002)** reported that experimental investigations of the luminescent properties of two different conjugated polymers in which we embedded nano crystals of Al_2O_3, Y_2O_3, ZnO, and SnSbO. The dielectric nano crystals result in a blue shifting and broadening of luminescence spectra of poly (*p*-phenylene vinylene with a simultaneous disappearance of its vibronic structure. The same nano crystals in a poly [2-(6-cyano-6'-methylheptyloxy)-

1, 4-phenylene] matrix cause red shifting and spectral broadening. These observations are explained by referring to a model that accounts for the change in the polarization component of the carrier and exciton energy in the vicinity of inclusions.

4. **Wei Xiang Chen *et al.,* (2003)** were prepared nano composites of carbon nanotubes (CNTs) with Sb and $SnSb_{0.5}$ particles by chemical reduction of $SnCl_2$ and $SbCl_3$ precursors in the presence of CNTs. SEM and TEM imaging showed that the Sb and $SnSb_{0.5}$ particles are uniformly deposited on the CNT exterior and in the CNT web. These CNT–metal composites are active anode materials for lithium ion batteries, showing improved cyclability compared to unsupported Sb and Sn–Sb particles and higher reversible specific capacities than CNTs. The reversible capacities were as high as 462 mAh/g for CNT–36 wt. % Sb and 518 mAh/g for CNT–56 wt. % $SnSb_{0.5}$. After 30 cycles, the capacity was 62.1% of the initial capacity for the former and 67.2% of the initial capacity for the later. In comparison Sb and $SnSb_{0.5}$ could only retain 17.7 and 23.5%, respectively of their initial capacities in the same number of cycles. The improvement in cyclability may be attributed to the nanoscale dimension of the metal particles and CNT's role as a buffer in relieving the mechanical stress induced by specific volume changes in electrochemical lithium insertion and extraction reactions.

5. **Vasilev V. P (2003)** studied the Sn–Sb system by the electromotive force method and the microstructural, X-ray diffraction, differential thermal, and microprobe analysis methods. Phenomenological crystal chemical models of the β phase were suggested. The models were based on hexagonal polymorph transformation into a quasicubic polymorph with a change in crystal symmetry corresponding to a second-order phase transition. The thermodynamic properties of the system were optimized.

6. **Christin Walle *et al.,* (2003)** have been studied the phase relations in the Au–Mn–Sb system by powder X-ray diffraction, metallography, electron microprobe analysis, and thermal analysis. The condensed phases occurring, tie-lines, and tie-triangles are presented for an isothermal section of the phase diagram at 400ºC. At this temperature the solid solubility of the third component in the binary phases is generally limited to a few percent. The

phase relations are relatively complex in regions which involve the numerous binary gold–manganese phases. The only genuine ternary phase, AuMnSb, has a very narrow composition range around Au_{35} Mn_{30} Sb_{35} and is stable up to 575± 5°C, where it decomposes peritectically. The AuMnSb phase is ferromagnetic with a Curie temperature of 135± 10 K. The solid-solution phase $AuMnSn_{1-x}$ Sb_x exhibits ferromagnetic properties throughout the entire homogeneity range with the Curie temperature ranging between 625 ±100 and 135 ±10 K.

7. **Zhufeng HOU *et al.*, (2004)** recent investigations SnSb has attracted in great attention as an anode material for Li ion batteries. The formation energies and electronic properties of the first-principles pseudo potential technique. The changes of volumes, band structures and charge density of states for the Li intercalations are presented. The results show that the average Li intercalation formation energy per Li atom is around 2.7 eV.
8. **Shchurova T *et al.*, (2005)** The valence-band maximum, the conduction-band minimum,, the position of the electronic states in quasi band gap formed by homopolar Sb-Sb bonds and clusters S_n for chalcogenide glassy alloys of Sb_xS_{1-x} ($0.35 \leq x \leq 0.45$) family have been calculated on the basis of the method suggested by W.A. Harrison. Spectral dependences of the photoelectron quantum yield, absorption coefficient, photoluminescence and photoconduction for $Sb_{0.40}$ $S_{0.60}$ have been presented. The photoemission threshold, the optical band gap, and the energies of the radiative and band-to-band transitions have been determined from these dependences, respectively. The experimental and calculated energy parameters have been correlated. Have been given experimental and calculated concentration dependences of the optical band gap, thermal activation energy and energy position of the peak in photoconduction spectra for $Sb_{0.35}$ $S_{0.65}$, $Sb_{0.38}$ $S_{0.62}$, $Sb_{0.40}$ $S_{0.60}$, $Sb_{0.43}$ $S_{0.57}$, and $Sb_{0.45}$ $S_{0.55}$.
9. **Xuan H.C *et al.*, (2007)** were prepared a series of $Ni_{43}Mn_{46}Sn_{11-x}$ Sb_x (x = 0, 1, and 3) alloys by an arc melting method. The martensitic transition shifts to higher temperature with the increasing Sb content. The isothermal magnetization curves and Arrott plots around martensitic transition temperatures show a typical metamagnetic behavior. Under a low applied

magnetic field of 10 kOe, large magnetic entropy changes around the martensitic transition temperature are 10.4, 8.9, and 7.3 J/kg K, for x = 0, 1, and 3, respectively. Already discussed the origin of the large magnetic entropy changes and potential application for $Ni_{43}Mn_{46}Sn_{11-x}$ Sb_x alloys as working substances in magnetic refrigeration.

10. **Hu Xiaowu *et al.*, (2008)** has been investigated the directionally solidified microstructure of Sn-16%Sb hyperperitectic alloy at various solidification rates using a high-thermal gradient directional solidification apparatus. The results indicate that the solidification microstructure consists of hard primary intermetallic SnSb phase embedded in a matrix of soft peritectic β-Sn phase. The primary SnSb phase exhibits faceted growth with tetragonal or trigonal shapes. At the same time, the primary SnSb phase is refined with an increase in the solidification rate and dispersed more uniformly in the matrix of β-Sn phase. The volume fraction of the SnSb phase firstly decreases and then increases when the solidification rate increases in directional solidification of Sn-16%Sb hyperperitectic alloy.

11. **Dixie P. Gautreaux *et al.*, (2008)** have synthesized five new analogues of the β-$CeNiSb_3$ family and found to be LnNi (Sn, $Sb)_3$ and isostructural to the previously reported β-CeNiSb3. LnNi (Sn, $Sb)_3$ (Ln = Pr, Nd, Sm, Gd, or Tb) crystallizes**,** in the orthorhombic space group, Pbcm, with lattice parameters of a~12.9A˚, b~6.1A˚ , c~12.0A˚ . The structure consists of layers of nearly square nets of X (X = Sn/Sb) atoms and highly distorted NiX_6 octahedra. Lanthanide atoms are located between layers of X and NiX_6 octahedra. All analogues are metallic and experimental effective magnetic moments are in agreement with the respective Ln^{3+} calculated moments.

12. **Chithra P.G *et al.*, (2008)** was synthesized a new inorganic-organic ion-exchanger p-chlorophenol anchored onto tin antimonate (SnSbpCP), where features of the organic and inorganic components complement each other leading to the formation of a new solid state structure with new composite properties. This type of composite represents a new class of hybrid ion exchangers with good ion-exchange capacity, higher stability, reproducibility and selectivity for heavy metals. The characterization of the resin was carried out by determining the ion exchange capacity, elemental analysis, pH titration,

FT-IR spectra and thermal analysis (TGA). Chemical resistivity of these materials was assessed in several acidic, basic and organic media. The distribution coefficients (K_d) for 10 metal ions were determined in demineralised water. On the basis of difference in K_d values some important binary separations of metal ions were achieved.

13. **Bumb A *et al.*, (2008)** were synthesized ultra-small super paramagnetic iron oxide nanoparticles (SPIOs) by co precipitation of iron chloride salts with ammonia and then encapsulated with thin (~2nm) layers of silica. The particles size, diffraction pattern, surface charge and magnetic properties are have been characterized. This rapid and economical synthesis has a number of industrial applications; however, the silica-coated particles have been optimized for use in medical applications as MR contrast agents, biosensors, and DNA capturing, bioseparation and enzyme immobilization.

14. **Shokrollahi H *et al.*, (2009)** reported that magnetic alloys are the key to the future of the power electronics industry. The recent development of transformers, chokes, inductors, filters and the emergence of completely new technologies call for entirely new types of magnetic alloys prepared by mechanical alloying (MA) methods. Because of the high magnetization and low coercivity of the magnetic materials appeal to the properties and operating requirements of these applications. The MA method was used to prepared the magnetic properties of (Fe–Ni, Fe–Si, Fe–Co, Fe–Si–Ni and Fe–Si–B) are some of the most important magnetic iron-based alloys.

15. **Rong Yang *et al.*, (2010)** have been synthesized hollow nanospheres of Sn–Sb–Cu alloy composites via co-reduction of metal chlorides in aqueous alkaline solution without using any surfactants or solid templates. To account for the formation of the hollow nanostructures was proposed by a bubble assisted growth mechanism. The concentration of the reactants kinetically controls the nucleation rate of the alloy nuclei, making for the formation of the hollow nanospheres. Compared with the alloy nanoparticles, the hollow spheres exhibit relatively high electrochemical capacity and good cyclic retention when used as anode materials for lithium-ion batteries. The bubble assisted synthesis method can be readily explored for fabricating hollow nanostructure of other alloy system for functional material applications.

16. **Kuok Hau Seng *et al.*, (2011)** was prepared SnSb/graphene porous three dimensional (3-D) composite with dual buffering capability by a chemical reduction of $SnCl_2$, $SbCl_3$, and graphene oxide prepared using a modified Hummers' method. The cyclic voltammetry and galvanostatic charge/discharge testing were investigated electrochemical performances of the SnSb/graphene composite. The SnSb/graphene composite delivered 688 mAh/g at the 2nd cycle (compared to a calculated theoretical value of 768 mAh/g) and capacity retention of 420 mAh/g after 100 cycles are shows good. A reaction model to explain the dual buffering effects of SnSb/graphene composite as anode material for lithium insertion and extraction has been proposed.

17. **Sougrati M. T *et al.*, (2011)** reported that electrochemical study of TiSnSb towards Li, as a negative electrode for Li-ion batteries. TiSnSb can reversibly take up more than 5 lithium's per formula unit leading to reversible capacities of 540 mA h g^{-1} and 4070 mA h cm^{-3} at 2C rate. From complementary operando XRD and Mossbauer spectroscopy measurements, it was shown that during the first discharge the TiSnSb undergoes a conversion process leading simultaneously to the formation of Li–Sb and Li–Sn alloys. Li_3Sb and Li_7Sn_2 were identified at the end of the discharge. Once the first discharge is achieved, both phases were shown to form Ti–Sn or Ti–Sb or Ti–Sn–Sb nano composites. Maintaining 90% of the specific capacity during 60 cycles at 2 C rate of cycling performance of TiSnSb was shown to be excellent. The good electrochemical performance of TiSnSb (compared to Sn and Sb) seems to be a consequence of the presence of the non-active metal. The comparative study of Ti/Sn/Sb composite demonstrated that the structural feature of the pristine material clearly impacts both the mechanism involved during the cycling and the corresponding performance.

Experimental regarding Co doping SnSb to prove magnetization was carried out by only a single person. In order to prove magnetization by Co doping SnSb the experimental based on this concept is carried out my project.

2.2 References

1. P. C. Schmidt, D. Stahl, B. Eisenmann, and R. Kniep, and V. Eyert and J. Kubler; Electronic Structure of the Layered Compounds K[SnSb], K[SnAs] and Sr[Sn,As]; Journal of solid state chemistry; 97;93-104; 1992.
2. Robert Lam, Jingjun Zhang,1 and Arthur Mar2; Ternary Antimonide EuSn3Sb4 and Related Metallic Zintl Phases**;** Journal of Solid State Chemistry; 150; 371-376; 2000.
3. S. Musikhin, L. Bakueva, E. H. Sargent, and A. Shik; Luminescent properties and electronic structure of conjugated polymer-dielectric nanocrystal composites; Journal of applied physics; 91(10); 6679-6683; 2002.
4. Wei Xiang Chen, Jim Yang Lee, Zhaolin Liu; T he nanocomposites of carbon nanotube with Sb and $SnSb_{0.5}$ as Li-ion battery anodes; Carbon; 41; 959–966; 2003.
5. V. P. Vasil'ev; A Complex Study of the Phase Diagram of the Sn–Sb System; Journal of Physical Chemistry; 79(1); 20–28; 2003.
6. Christin Walle, Laila Offernes, A. Kjekshus; T he ternary system Au–Mn–Sb and the AuMnSnSb phase; Journal of Alloys and Compounds; 349; 105–110; 2003.
7. Zhufeng Hou, Aiyu Li, Zizhong Zhu, Meichun Huang and Yong Yang; Ab initio Calculations of the formation energies of lithium interactions in SnSb; Journal of material science technologies; 20(6); 743-745; 2004.
8. T. Shchurova, N. Savchenko, V. M. Rubisha, V. V. Rubish, A. Spesivykh, I.Opachkop; Electrical and optical properties of Sb_xS_{1-x} alloys; Journal of Optoelectronics and Advanced Materials ; 7(4); 2021 – 2027; 2005.
9. H.C. Xuan, D.H. Wang, C.L. Zhang, Z.D. Han, H.S. Liu, B.X. Gu, Y.W.; The large low-field magnetic entropy changes in $Ni_{43}Mn_{46}Sn_{11-x}Sb_x$ alloys; Solid State Communications; 142;591–594; 2007.
10. Hu Xiaowu, Li Shuangming, Liu Lin, Fu Hengzhi; Microstructure evolution of directionally solidified Sn-16%Sb hyperperitectic alloy; Research & Development; 5(3); 167-171; 2008.

11. Dixie P. Gautreaux a, Cigdem Capan b, John F. DiTusa b, David P. Young b, Julia Y. Chan; Synthesis, structure and physical properties of $LnNi(Sn,Sb)_3$ (Ln ¼ Pr, Nd, Sm, Gd, Tb); Journal of Solid State Chemistry; 181 ; 1977–1982; 2008).
12. P.G. Chithra, R. Raveendran, B. Beena; Parachlorophenol anchored tin antimonite- an inorganic-organic ion-exchanger selective towards heavy metals like Bi(III) and Cu(II); Desalination; 232 ; 20–25; 2008.
13. A Bumb, M W Brechbie, P L Choyke, L Fugger, A Eggeman, D Prabhakaran, JHutchinson, and P J Dobson; Synthesis and characterization of ultra-small superparamagnetic iron oxide nanoparticles thinly coated with silica; Nanotechnology; 19(33); 335601; 2008.
14. H. Shokrollahi; The magnetic and structural properties of the most important alloys of iron produced by mechanical alloying; Materials and Design; 30; 3374–3387; 2009.
15. Rong Yanga, Jing Huanga, Wei Zhao, Wenzhong Lai, Xuanzhou Zhanga, Jie Zhenga, Xingguo Li; Bubble assisted synthesis of Sn–Sb–Cu alloy hollow nanostructures and their improved lithium storage properties; Journal of Power Sources; 195; 6811–6816; 2010.
16. Kuok Hau Seng, Zai Ping Guo, Zhi Xin Chen, and Hua Kun Liu; SnSb/Graphene Composite as Anode Materials for Lithium Ion Batteries; Advanced Science Letters; 4; 18–23; 2011.
17. M. T. Sougrati, J. Fullenwarth, A. Debenedetti, B. Fraisse, J. C. Jumas and L. Monconduit ; TiSnSb a new efficient negative electrode for Li-ion batteries: mechanism investigations by operando-XRD and Mossbauer techniques; Journal of Materials Chemistry; 21; 10069; 2011.

CHAPTER-III

SYNTHESIS AND EXPERIMENTAL TECHNIQUES

3.1 Introduction

This chapter describes the experimental techniques used in the preparation and characterization of nano alloy, Sn_xSb_y- pure and doped with transition metal Co in the composition. The method of preparation is reduction co-precipitation technique. The various experimental techniques such as X-ray Diffraction (XRD), Scanning Electron Microscope (SEM), Energy Dispersive X-ray Analysis (EDX), Fourier Transform Infrared Spectroscopy (FTIR), Photoluminescence (PL), Photoluminescence Emission (PLE) studies have been employed to understand details of phase, grain morphology and electronic levels.

3.2 Wet Chemical Method

There is variety of methods found in the literature. To prepare thin alloy namely, liquid phase sol-gel process, hydrothermal synthesis [1], spray drying [2], aerosol spray pyrolysis [2] etc.

3.2.1 Raw Materials Method

There are seven raw materials are used:

- Tin chloride ($SnCl_2$)
- Antimony chloride($SbCl_3$)
- Tri Sodium citrate ($C_6H_5Na_3O_7$)
- Sodium boro hydride ($NaBH_4$)
- Sodium hydroxide (NaOH)
- Hydrochloric acid (HCl)
- Acetone

The $NaBH_4$ is used as reducing agent and absorbs a proton. It reduces aldehydes and ketones into alcohols. The NaOH is used as the precipitating agent in the solution. The NaOH will release hydroxyl ions (OH^-). The distilled water is used as the solvent.

3.2.2 Preparation Method

There are four steps:

Step 1: We have take the appropriate gram molecular weights of $SnCl_2$ and $SbCl_3$ and $C_6H_5Na_3O_7$ (tri sodium citrate) dissolved in distilled water. The solution is stirred well for 30 minutes in a magnetic stirrer. Thus solution A is arrived at.

Step 2: We have take the appropriate gram molecular weights of NaOH and $NaBH_4$ and dissolved water. The solution is stirred well for 30 minutes in a magnetic stirrer. Thus solution B is obtained.

Step 3: The solution A is mixed drop by drop into solution B. The solution dissolved completely in 45 minutes with vigorous and continuous stirring all the way through to ascertain homogeneity.

Step 4: The solution was filtered with Whattman filter paper following by washing with distilled water, dilute HCl, distilled water and acetone.

The succeeding sample with SnSb composition is prepared by the above method and characterized.

3.2.3 Preparation of Transition Metal (Co) Added Sn_xSb_y Alloy Powders

To include the transition metal like $CoCl_2$ is added to solution A and the preparation was carried out reductive co-precipitation. Only one composition of nano sized Sn_xSb_y; Co alloy powder is prepared by reductive precipitation method and its characterizations are explained.

3.3 Structural and morphological studies

3.3.1 X–ray Powder Diffraction (XRD)

X-ray powder Diffraction (XRD) is a rapid analytical technique primarily used for phase identification of a crystalline material and can provide information on unit cell dimensions. It is very important technique that has long been used related to the crystal structure of solids, including lattice constants and geometry, orientation of single crystals, defects, stresses, etc.

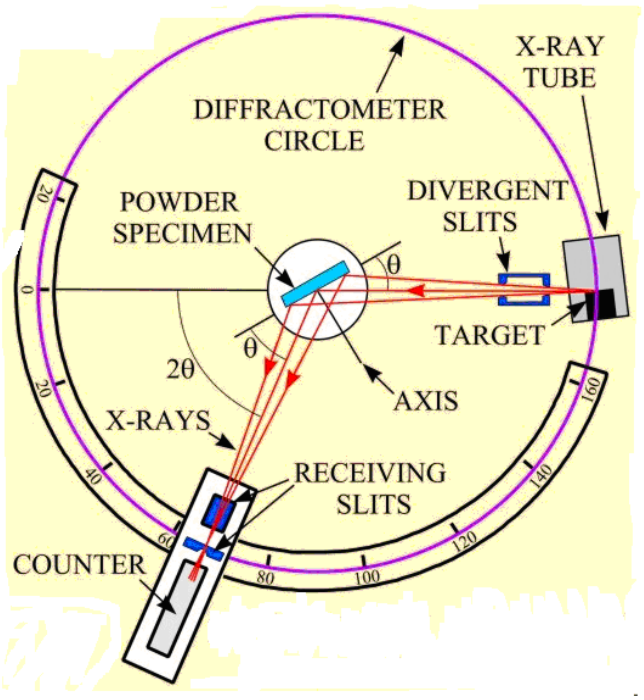

Figure 3.1 Schematic diagram of X-ray Diffractometer

Principles of X-ray Diffraction

Diffraction effects are observed when electromagnetic radiation impinges on periodic structures with geometrical variations on the length scale of the wavelength of the radiation. The interatomic distances in crystals and molecules amount to 0.15 - 0.4nm which correspond in the electromagnetic spectrum with the wavelength of X-rays having photon energies between 3 and 8 keV. Accordingly, phenomena like constructive and destructive interference should become observable when crystalline and molecular structures are exposed to X-rays.

Figure 3.2 Schematic representation of XRD

Samples

The X-ray diffraction is mainly used for “finger print identification” of various solid materials. In powder diffraction, it is important to have a sample with a smooth plane surface. If we normally grind the sample down to particles of about 0.002mm to 0.005mm cross section. The ideal sample is homogeneous and the crystallites are randomly distributed. The sample is pressed into a sample holder so that we have a smooth flat surface. In X-ray diffraction, the sample holder is made for aluminium plate.

Only crystallites having reflecting planes (h, k, l) parallel to the specimen surface will contribute to the reflected intensities. If have a truly random sample, each possible reflection from a given set of h, k, l planes have an equal number of crystallites contributing to it. Only have to rock the sample through the glancing angle THETA in order to produce all possible reflections. The diffraction grains are recorded and analyzed for phase identification, JCPDS (ICDD) data is compared to confirm the phase formation.

Bragg's Formula

In XRD, a collimated beam of X-rays, with a wavelength typically ranging from 0.7 to 2 Å, is incident on a specimen and its diffracted by the crystalline phases in the specimen according to Bragg's law,

$$\lambda = 2d \sin\theta$$

Where,

d→ is the spacing between atomic planes in the crystalline phase and

λ →is the X-ray wavelength.

The intensity of the diffracted X-ray is measured as a function of the diffraction angle 2θ and the specimens orientation. This diffraction pattern is used to identify the specimens crystalline phases and to measure its structural properties. X-ray diffraction is nondestructive and does not require elaborate sample preparation, which partly explains the wide usage of X-ray diffraction method in materials characterization.

Scherrer's Formula

If there is no homogeneous strain, the crystallite size, D, can be estimated from the peak width with the Scherrer's formula [3],

$$D = k \lambda / \beta \cos\theta$$

Where,

λ → is the X-ray wavelength,

B→ is the full width of height maximum (FWHM) of a diffraction peak,

θ→ is the diffraction angle,

k → is the scherrer's constant of the order of unity.

In addition, X-ray diffraction only provides the collective information of the particle sizes and usually requires a sizable amount of powder. This technique is very useful in characterizing nanoparticles. The film thickness of exptaxial and highly textured thin films can also be estimated with X-ray diffraction [4].

3.3.2 Scanning Electron Microscope (SEM)

Scanning Electron Microscope (SEM) is a type of electron microscope that produce image of a sample by scanning it with a focused beam of electrons. The Scanning Electron Microscope (SEM) uses a focused electron beam which is scanned on the surface of the sample to produce high quality images of the surface topography. Scanning Electron Microscope (SEM) essentially offers a very high resolution capabilities and a large depth of focus.

It is one of the most widely used techniques used in characterization of nanomaterials and nano structures. Scanning Electron Microscope approaches a few nanometers and the instruments can operate at magnifications that are easily adjusted from ~ 10 to over 300,000. The Scanning Electron Microscope produce topographical information, it also provides the chemical deposition information near the surface. Typically Scanning Electron Microscope, a source of electrons is focused into a beam, with a very fine spot size and having energy ranging from a few eV to KeV that is rastered over the surface of the specimen by deflection coils.

The electrons strike and penetrate the surface, a number of interactions occur that result in the emission of electrons and photons from the sample, and Scanning Electron Microscope images are produced by collecting the emitted electrons on a cathode ray tube (CRT). Various Scanning Electron Microscope techniques are differentiated on the basis is subsequently detected and imaged and the principle images produced in the Scanning Electron Microscope are of three types:1) Secondary electron images, 2) Backscattered electron images and 3) Elemental X-rays maps. An electron interaction in the Scanning Electron Microscope is that the primarily electron collides with and ejects a core electron from an atom in the sample. The excited atom will decay to its ground state by emitting either a characteristic X-ray photon or an atom auger electron, both of which have been used for chemical characterization. Combining with chemical analytical capabilities, Scanning Electron Microscope provides the image of the morphology and nanostructured materials and devices, but can also provide detailed information of chemical deposition and distribution.

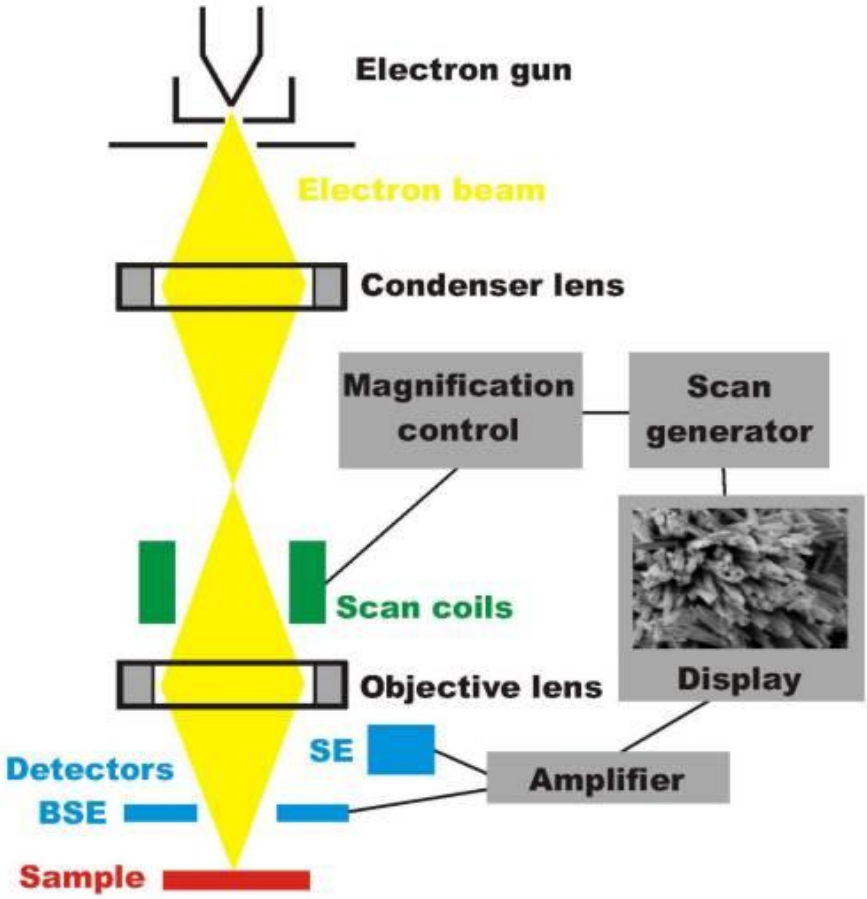

Figure 3.3 Schematic diagram of SEM instrument

The theoretical limit to an instruments resolving power is determined by the wavelength of the electron beam used and the numerical aperture of the system. The resolving power, R_1 of an instrument is defined as:

$$\mathbf{R = \lambda / 2NA}$$

Where,

$\lambda \rightarrow$ wavelength of electrons,

NA$\rightarrow$ is the numerical aperture which is engraved on each objective and condenser lens system, and a measure of the electron gathering ability of the objective, or the electron providing ability of the condenser [5].

3.3.3 Energy Dispersive X-ray Analysis (EDX)

Energy Dispersive X-ray Analysis (EDX) is an analytical technique used for the elemental analysis or chemical characterization of a sample. The number or energy of the X-rays emitted from a specimen can be measured by an energy dispersive spectrometer. Energy Dispersive X-ray Analysis (EDX), referred to as EDS or EDAX, is an X-ray technique used to identify the elemental composition of materials. Applications include materials and product research, trouble shooting, deformulation and more.

In multi technique approach Energy Dispersive X-ray Analysis (EDX) becomes very powerful, particularly in contamination analysis and industrial forensic science investigation. The technique can be qualitative, semi-qualitative, and quantitative and also provide spatial distribution of elements through mapping. It makes a model of **JEOL-model 6390** and specimen size is **8mm to 150 mm**.

Figure 3.4 Schematic representation of Energy Dispersive X-ray Analysis

3.4 Optical studies

3.4.1 Fourier Transform Infrared Spectroscopy (FTIR)

Fourier Transform Infrared Spectroscopy (FTIR) is a technique which is used to obtain an infrared spectrum of absorption, emission of a solid, liquid or gas. A Fourier Transform Infrared spectroscopy (FTIR) Spectrometer simultaneously collects spectral data in a wide spectral range. Fourier Transform Infrared Spectroscopy (FTIR) is a measurement technique where by spectra are collected

based on measurement of the coherence of a radiative source , using time-domain or space domain measurement of the electromagnetic radiation or other type of radiation.

Figure 3.5 Schematic representation of FTIR

In Infrared Spectroscopy, IR radiation is passed through a sample. Some of the infrared radiation is absorbed by the sample and some of it pass through (get transmitted). The resulting spectrum the molecular absorption and transmission creating a molecular finger print of the sample. Fourier Transform Infrared Spectroscopy (FTIR) is the most useful technique for identifying chemicals that are either organic or inorganic. It can be utilized to quantitative some components of an unknown mixture. It can be applied to the analysis of solids, liquids or gases. The term Fourier Transform Infrared Spectroscopy (FTIR) refers to a fairly recent development in the manner in which the data is collected and converted from an interference pattern to a spectrum. **KBr pellet** is used and company name is **Sigma Aldrich** and **IRAffinity-1** and company model is **SHIMADZU**.

Sample Analysis Process

- The Source
- The Interferometer
- The Sample
- The Detector
- The Computer

Sample Preparation

Solid samples can be milled with Potassium Bromide (KBr) to form a very fine powder. This powder is then compressed into a thin pellet which can be analyzed. KBr is having a transparent window in the IR region. The infrared spectra can be divided into three parts:

1) near infrared region → 14290-4000 cm^{-1}
2) mid infrared region → 4000-700 cm^{-1}
3) far infrared region →700-200 cm^{-1}

3.5 References

1. J.He, H.Zhao, J.Wang, J.Chen; Hydrothermal synthesis and electro thermal properties of nanosized Co Sn alloy anodes for lithium ion batteries; Journal of alloys and compounds; 508(2); 629-635; 2010.
2. R.G.Haverkamp; A Decade of nanoparticle research in Australia and Zealand; Particulate Science and Technology; 28(1); 1-40; 2010.
3. L.S.Birks and H.Friedman; Journal of applied physics; 17; 687; 1946.
4. A.Segmuller and M.Murakami; in thin films from free atoms and particles, ed. K.J.Klabunde; Academic press, Orlando, FL; 325; 1985.
5. S.J.Limmer, S.Vince Cruz and G.Z.Cao; Advanced Material; 2003.
6. C.R.Kagan, C.B.Murray, and M.G.Bawendi; physics Rev.B54; 8633; 1996.
7. Al.L.Efros and M. Rosen; Ann. Rev. Mater.Science; 30; 475; 2000.

CHAPTER –IV

RESULTS AND DISCUSSION

4.1 Introduction

This chapter deals with the results of various Sn_xSb_y (x: y =2:3, 3:2, 3:4, etc.) compositions. The aim of the work is to study the Sn_xSb_y nano alloy and the influence of the transition metal Co added alloy. The structural and morphological studies of the above said samples are discussed. The method of preparation is slow titration process.

4.2 Structural Characterization

4.2.1 X-ray Diffraction Analysis (XRD)

The prepared SnSb composition was investigated using X-ray diffraction in which it is used to determine the phase formation. The diffraction pattern plotted in Figure 4.1 shows the strong peaks, indicating the crystalline nature of rhombohedral SnSb nano alloy (ICDD #33-0118). There is no evidence to suggest the presence of any other metal or alloy phase. [1] in the X-ray Diffraction pattern of Sn_xSb_y compositions as prepared by reductive co-precipitation method. The aluminium peaks are excluded in the procedure. The sample ratios are prepared (a) 2:3, (b) 2:3 (Co=0.2), (c) 3:2, (d) 3:2, (e) 3:4, (f) 3:4(Co=0.2), (g) 3:4 (Co=0.5) for all the Sn_xSb_y compositions. The structures of all the samples are rhombohedral and the lattice constants are the same and the molecular weight is 240.44. The sharp peak gives low particle size and indicates the existence of nano size. In all the samples, the peaks at 29°, 41°, $51^{\circ}$and 60° correspond to the (101), (110), (003), (202) orientation and Sn cubic structure with the peak at 39º correspond to the (220) plane. It is identified that the Co substituted samples (f) and (g) were white in color due to the presence of Sb dominant over the Sn i.e., the Sn ratio is very low compared to Sb. The traces of Cl impurity is found in the samples f) and g) and the structure is Orthorhombic the 2θ = 26º correspond to the (111) direction. Hence Sb and Cl may be the reasons for the white color.

The ratios namely 2:3, 3:2, 3:4 and cobalt substitution of 0.2 and 0.5 Co are prepared. The preparation of 3:2 resulted in white powder at times and black at another time hence this has been taken as an indicative response to identify the phase

formation. Both black and white powder were analyzed. All the peak identification has been marked in the respective figures for the comfort of the reader. The Co substitution at 0.5% ratio ended with multiphase composition of cubic and rhombohedral structure. Hence all the other samples were loaded with 0.2% Co only.

Already Vasilev et.al.reported at these existences of a Sn_3Sb_2 phase has not been substantiated by X-ray diffraction thus far [2]. But from the sample (c) and (d) it has formed a single phase and the reason is varying the temperature. Table 4.1 shows the plane (hkl) assignments using the X-ray diffraction peaks obtained.

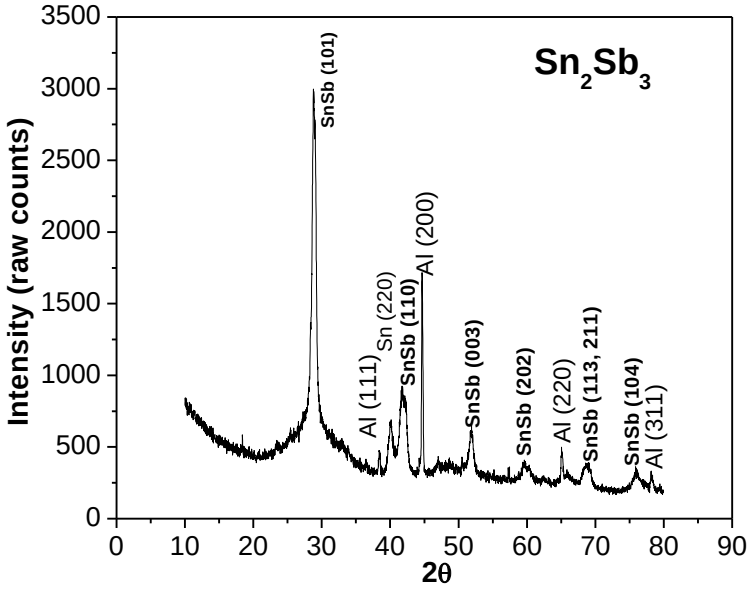

Figure 4.1 (a) XRD Pattern for Sn_xSb_y (x=2, y=3)

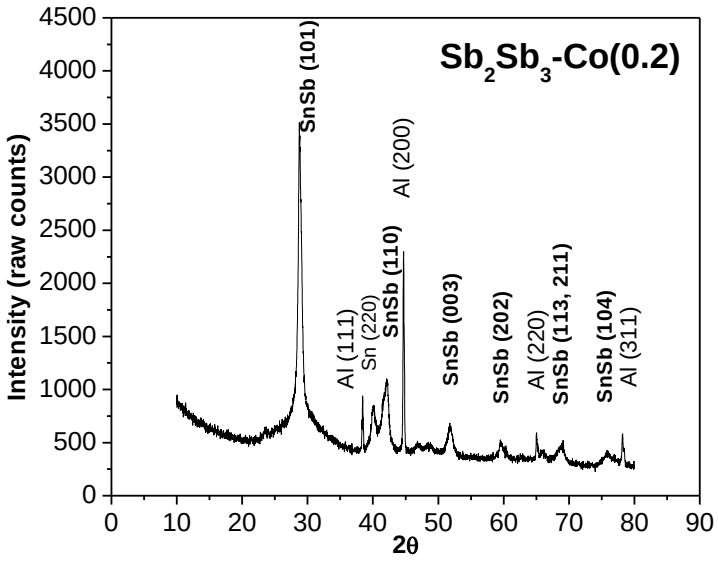

Figure 4.1 (b) XRD Pattern for Sn_xSb_y-Co (x=2 y=3)

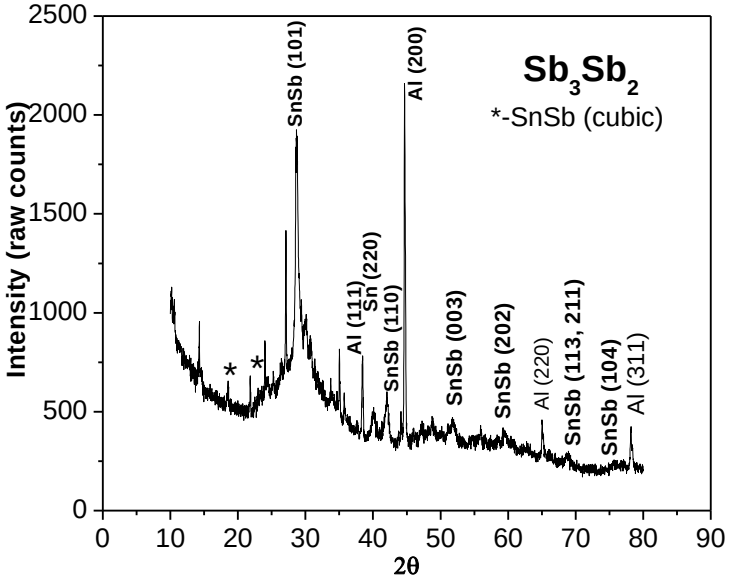

Figure 4.1 (c) XRD Pattern for Sn_xSb_y (x=3, y=2) with white color

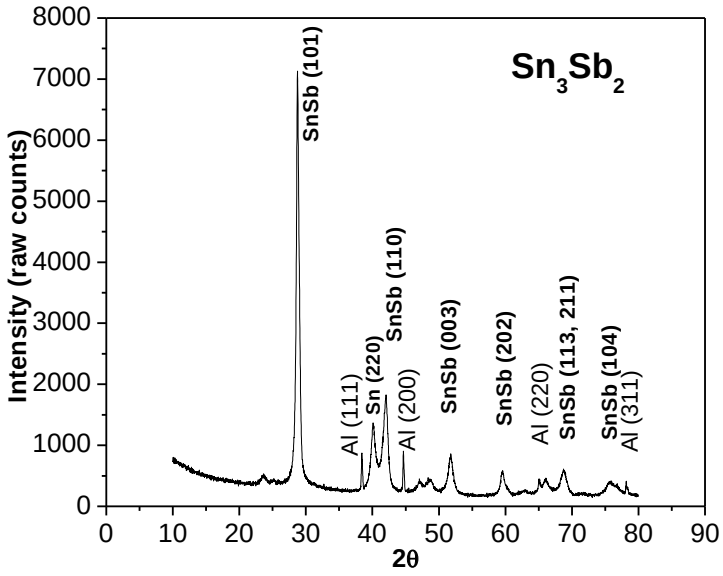

Figure 4.1 (d) XRD Pattern for Sn_xSb_y (x=3, y=2) with black color

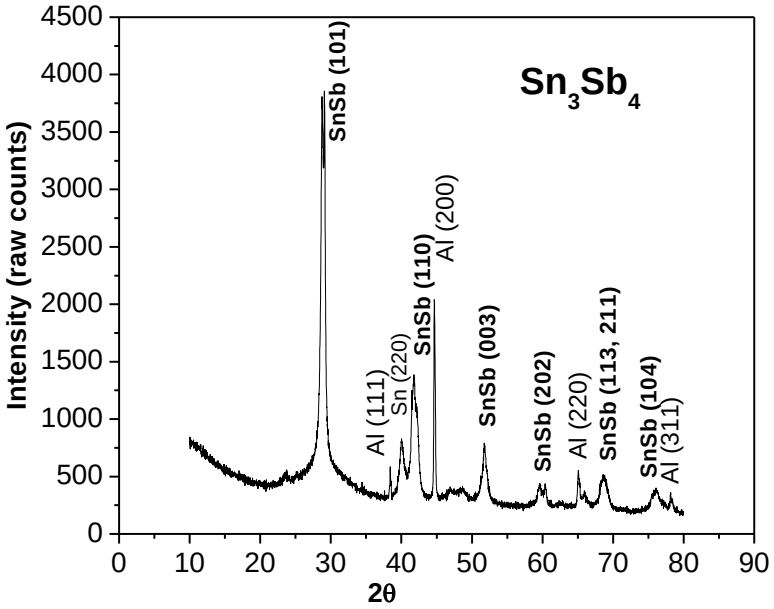

Figure 4.1 (e) XRD Pattern for Sn_xSb_y (x=3, y=4)

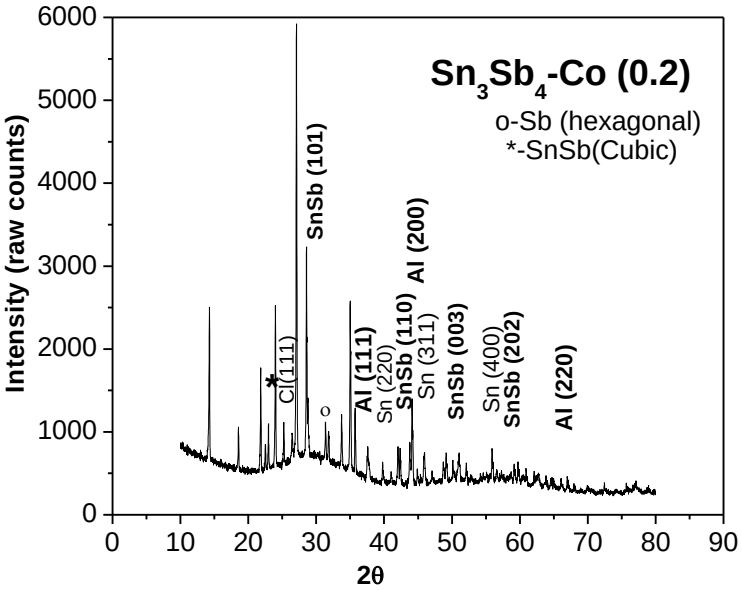

Figure 4.1 (f) XRD Pattern for Sn_xSb_y-Co (x=3, y=4)

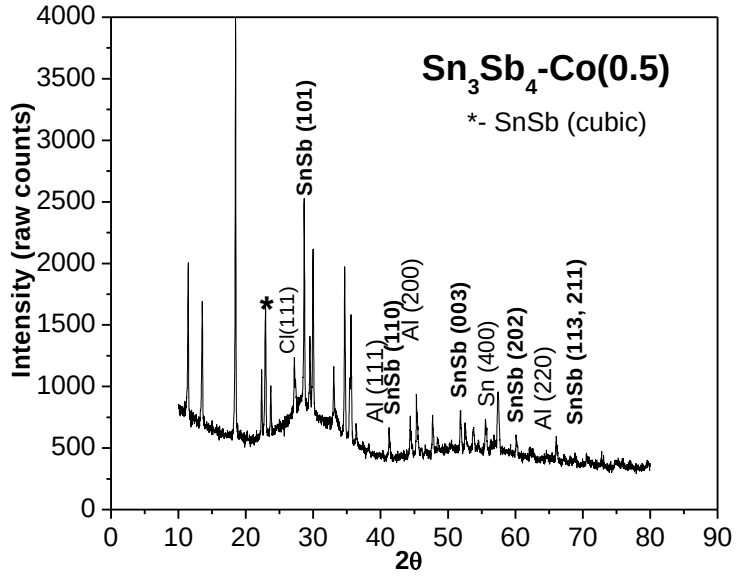

Figure 4.1 (g) XRD Pattern for Sn_xSb_y-Co (x=3, y=4)

Table 4.1 The different <hkl> planes assignment to the XRD peaks obtained

Sn_xSb_y (x=2, y=3) (Rhombohedral); lattice constants, a=4.325 Å and c=5.346 Å

No. of Peaks	2θ(deg)	h	k	l	$1/d^2$cal
1	29.09	1	0	1	0.1063
2	41.74	1	1	0	0.2112
3	51.17	0	0	3	0.3149
4	60.27	2	0	2	0.4250
5	68.10	1	1	3	0.3188
6	75.45	1	0	4	0.6311

4.2.2 Morphological Analysis

The Scanning Electron Micrographs of Sn_xSb_y-Co (x=2, y=3) composition is shown in Figure 4.2 (c). Scanning Electron Microscope shows that SnSb material is made of a distribution of shapeless grains. Several images are taken from different locations to arrive at the particle size from each sample. The particle sizes of Sn_xSb_y (x=2, y=3), Sn_xSb_y (x=3, y=2), Sn_xSb_y-Co (x=2, y=3), Sn_xSb_y (x=3, y=4), Sn_xSb_y-Co (x=3, y=4) are 33-350 nm, 33-250 nm, 33-200 nm, 33-200 nm, 156-781 nm respectively. The Sn_xSb_y compositions as prepared by reductive co-precipitation method and to obtain the sample Sn_xSb_y-Co (x=3, y=4) is very high grain size of 0.781 μm and 781 nm. In our case very high agglomeration is found in this sample only. Then enhanced electrostatic attraction between surfaces, leads to highest agglomeration in other words, indicates a decreased particle size [3]. Figure 4.3 (a), (b), (c), (d), (e) shows the size distribution analysis of all the samples. It is seen that majorly agglomerations of 15 μm size is found in 2:3, 5-10 μm in 3:2, 5-10 μm for Cobalt substituted 2:3, 10-15 μm in 3:4 and 5-20 μm in Cobalt substituted 3:4 samples. On total, a standard deviation of 7 in all the samples were present and has to be accounted in the analysis. Hence it is to be noted that the variation in agglomeration size is due to the phase changes and surfacial phenomena due to the particle size.

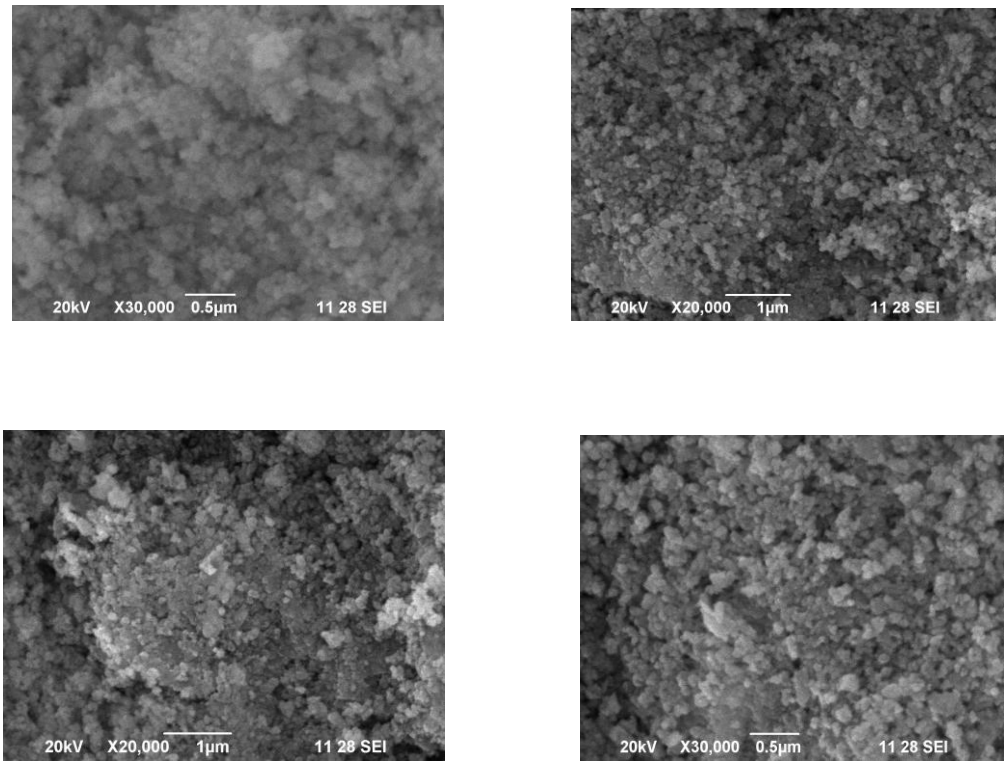

Figure 4.2 (a) SEM Images for Sn_xSb_y (x=2, y=3) composition

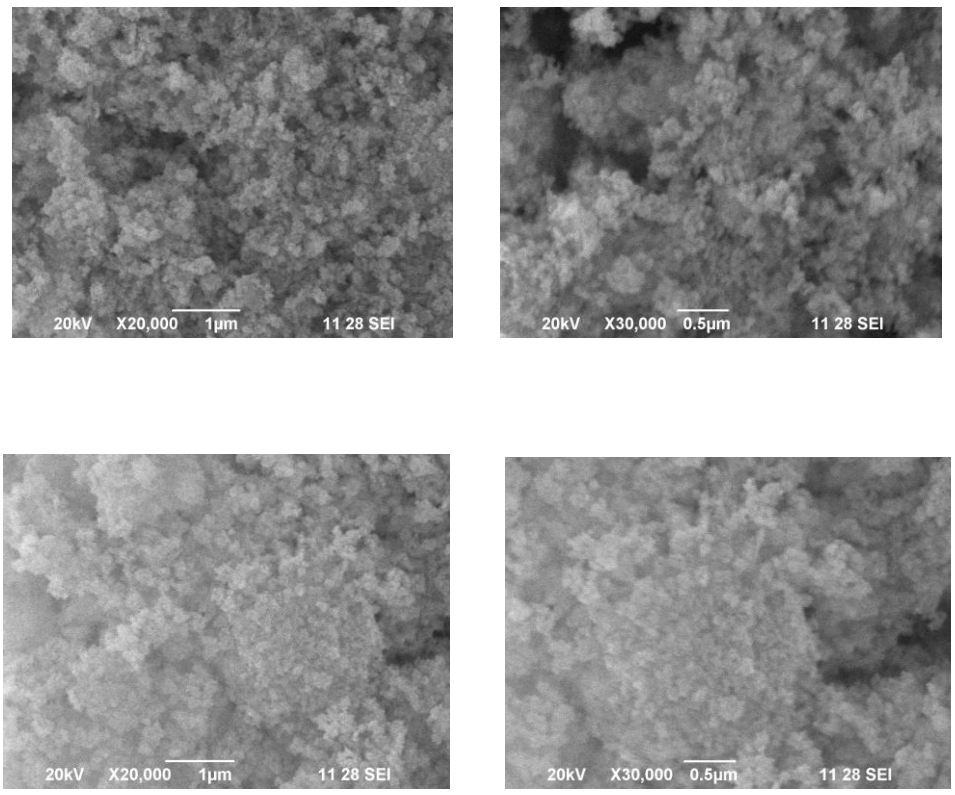

Figure 4.2 (b) SEM Images for Sn_xSb_y-Co (x=2, y=3) composition

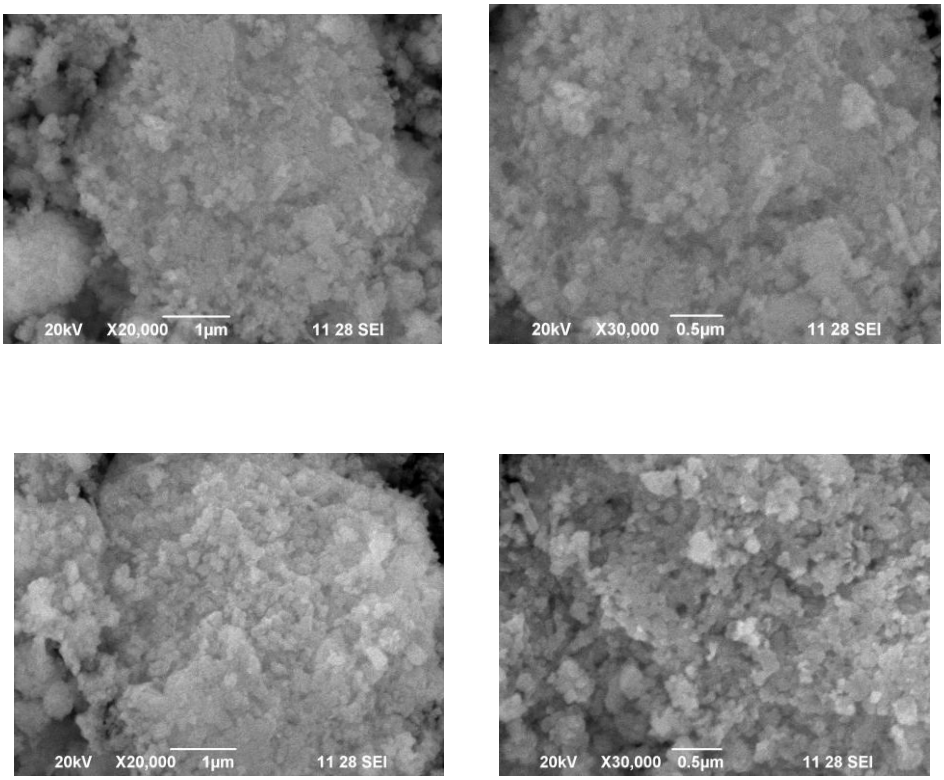

Figure 4.2 (b) SEM Images for Sn_xSb_y (x=3, y=2) composition

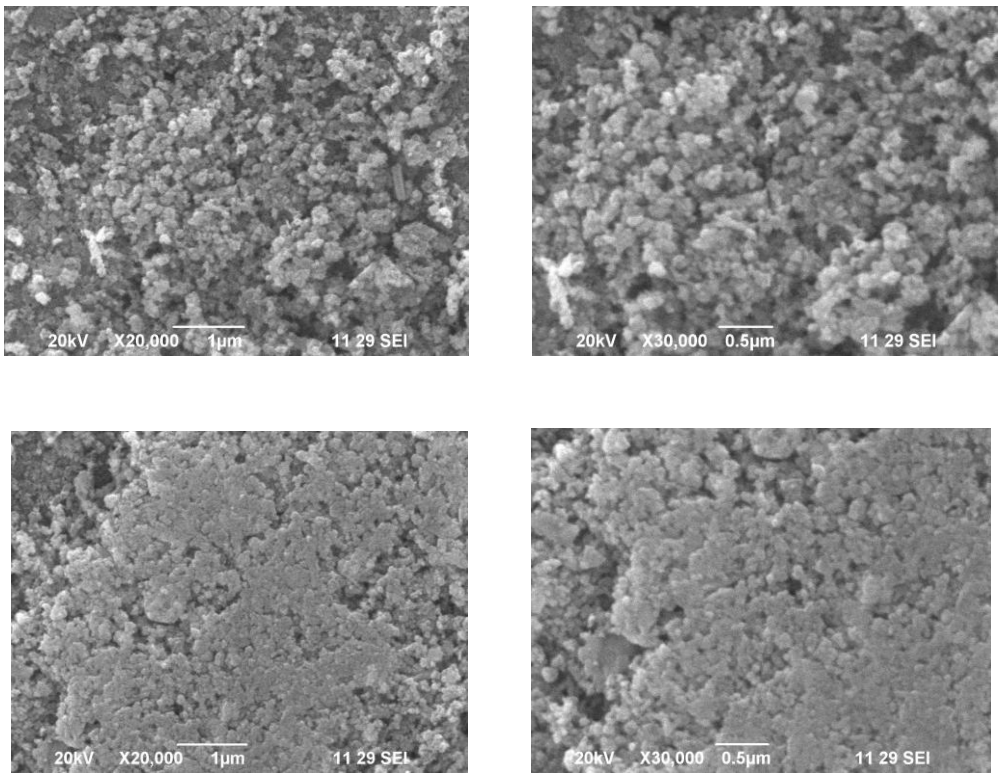

Figure 4.2 (d) SEM Images for Sn_xSb_y (x=3, y=4) composition

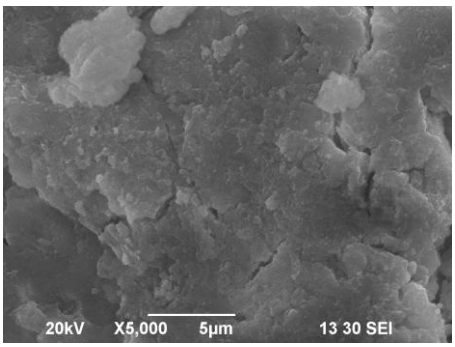

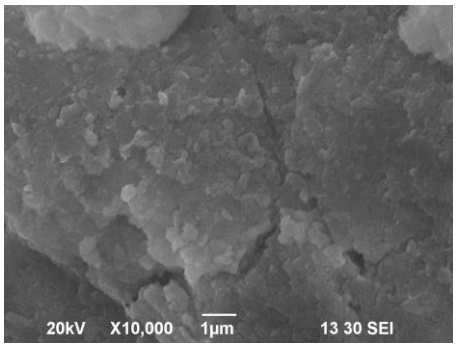

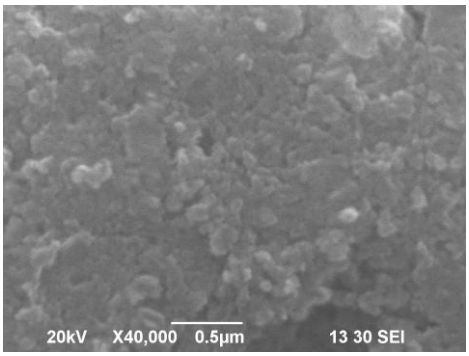

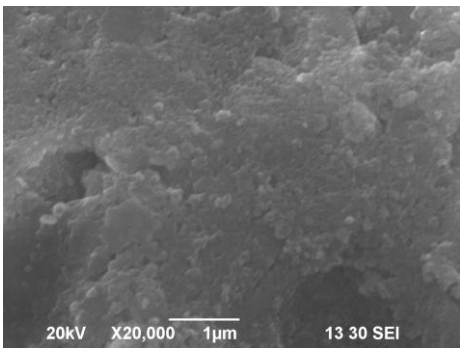

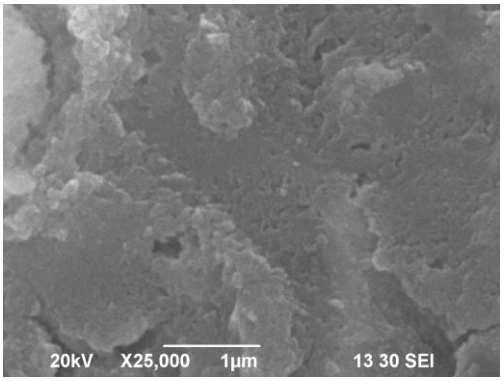

Figure 4.2 (e) SEM Images for Sn_xSb_y-Co (x=3, y=4) composition

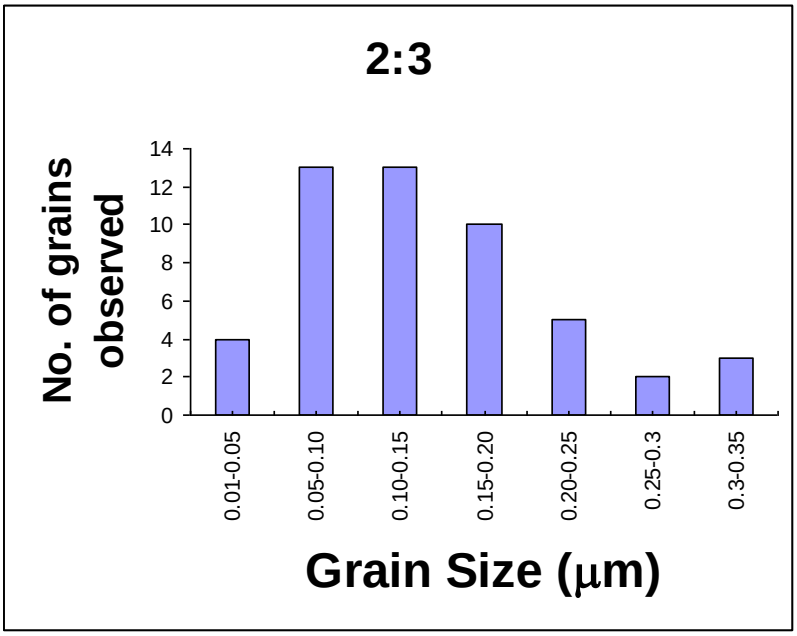

Figure 4.3 (a) Histogram of SEM in Sn_xSb_y (x=2, y=3) composition

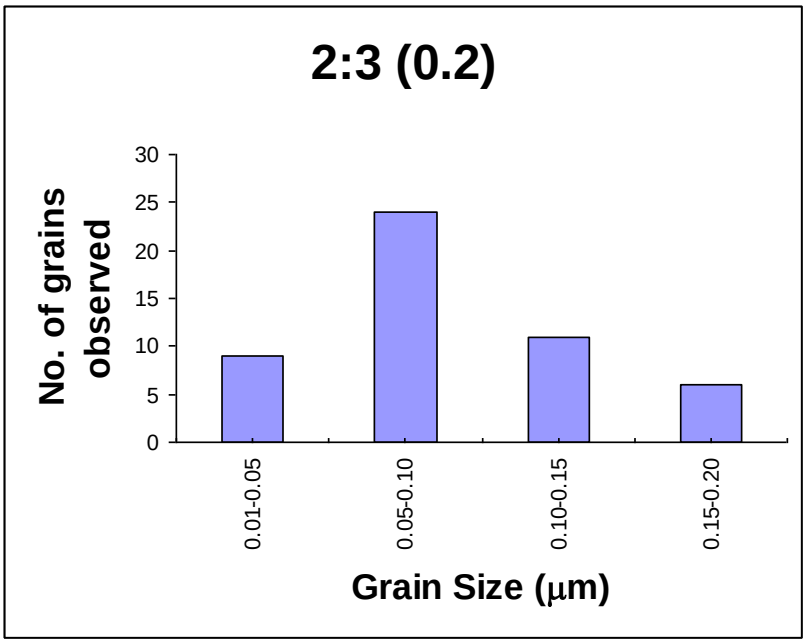

Figure 4.3 (b) Histogram of SEM in Sn_xSb_y-Co(x=2, y=3) composition

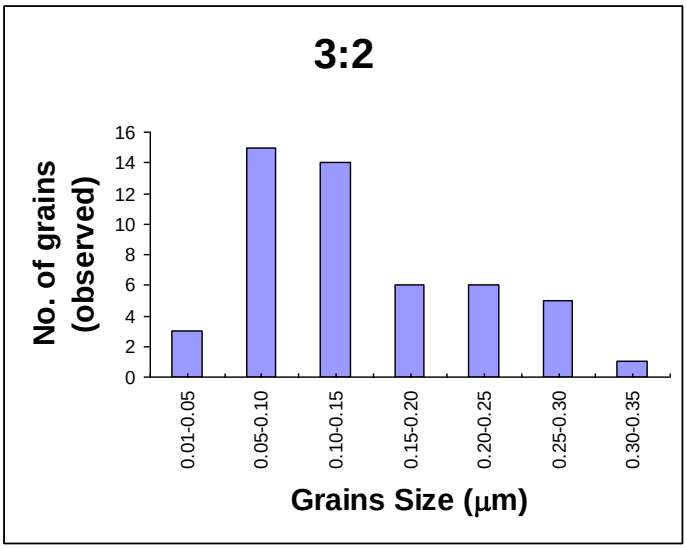

Figure 4.3 (c) Histogram of SEM in Sn_xSb_y (x=3, y=2) composition

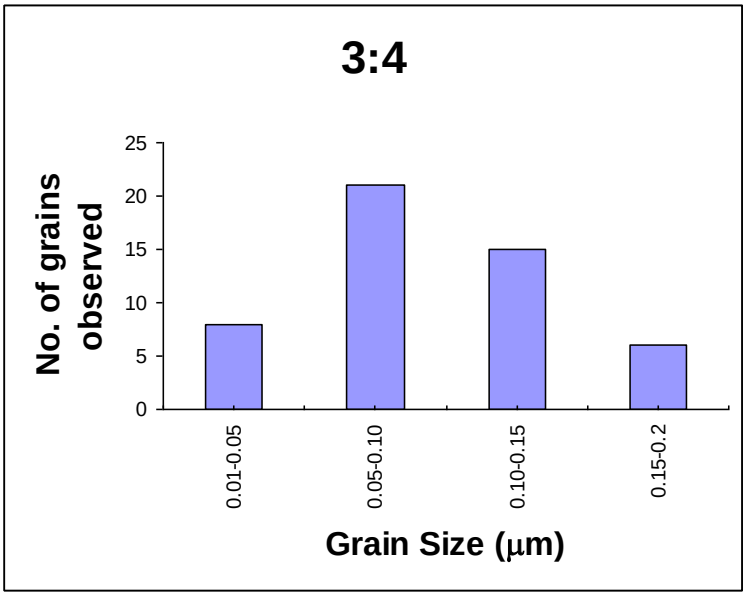

Figure 4.3 (d) Histogram of SEM in Sn_xSb_y (x=3, y=4) composition

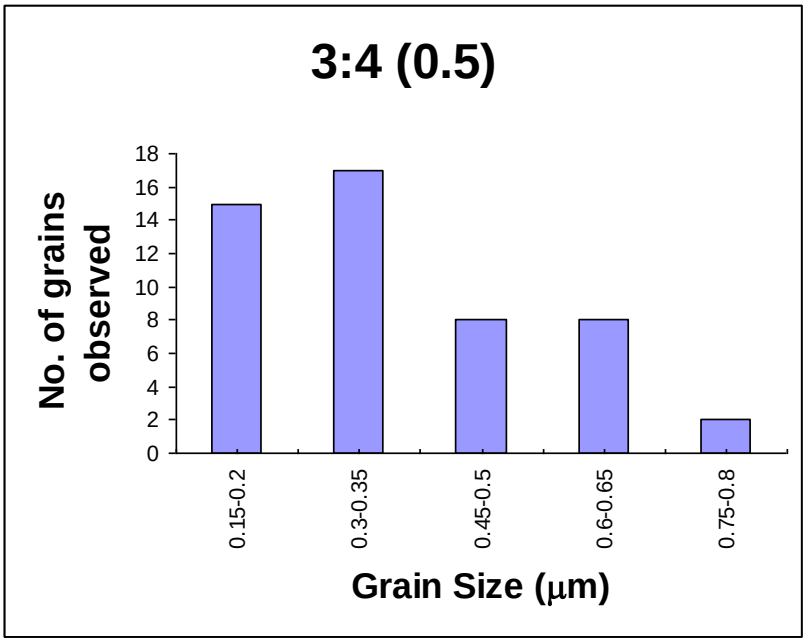

Figure 4.3 (e) Histogram of SEM in Sn_xSb_y-Co (x=3, y=4) composition

4.2.3 Energy Dispersive X-ray Analysis (EDX)

Figure 4.4 (b) shows that EDX analysis of Sn_xSb_y-Co(x=2, y=3) composition. The sample compositions are Sn_xSb_y (x=2, y=3), Sn_xSb_y-Co (x=2, y=3), SnxSby (x=3, y=2), Sn_xSb_y (x=3, y=4), Sn_xSb_y-Co (x=3, y=4). There are no peaks corresponding to impurity in all the Sn_xSb_y compositions. The samples atomic weight percentages are observed and the molecular formula is calculated as $Sn_{0.46}Sb_{4.49}$ (a), $Sn_{0.0318}Sb_{4.602}Co_{0.452}$ (b), $Sn_{0.0476}Sb_{4.878}$ (c), $Sn_{0.123}Sb_{6.803}$ (d), $Sn_{0.685}Sb_{5.323}Co_{1.424}$ (e). Energy Dispersive X-ray analysis was performed in order to analyze the elemental composition of the sample. The sample Sn_xSb_y-Co (x=2, y=3), Sn_xSb_y-Co (x=3, y=4) indicates the existence of Co, Sn and Sb in the sample, suggesting that Co has entered the Sn_xSb_y lattice [4]. The oxygen has been avoided in the calculation of molecular weight since the EDX has been carried out in low vacuum and the oxygen from the atmosphere may interfere in the estimation. Table 4.2 shows the atomic weight percentage of Sn, Sb and Co composites for all the samples.

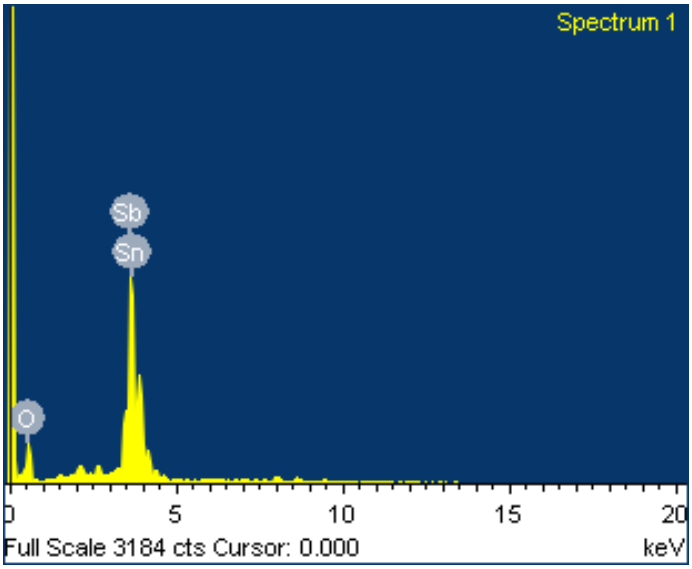

Figure 4.4 (a) EDX Image for Sn_xSb_y (x=2, y=3) composition

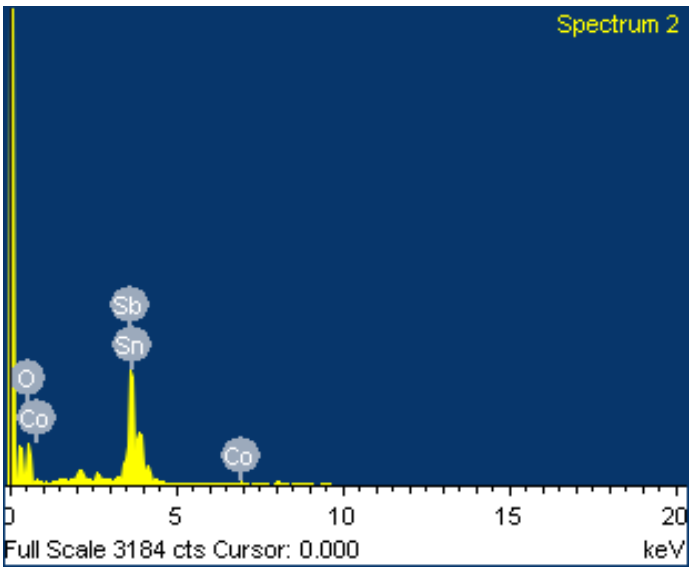

Figure 4.4 (b) EDX Image for Sn_xSb_y-Co(x=2, y=3) composition

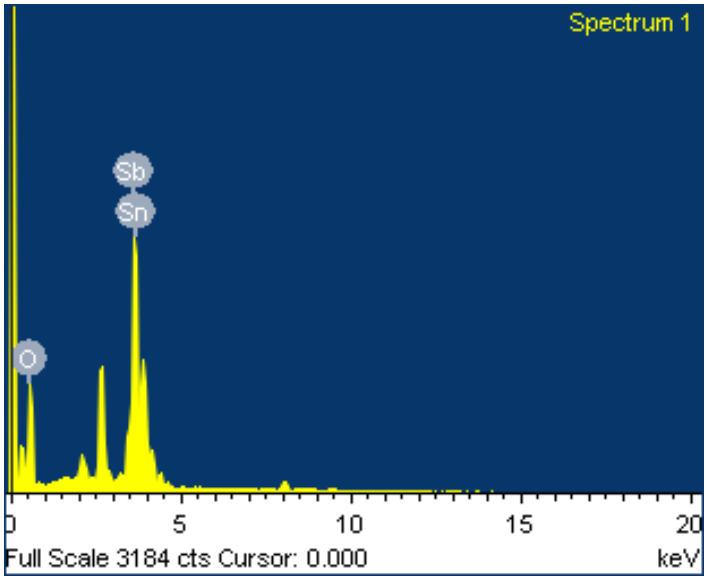

Figure 4.4 (c) EDX Image for Sn_xSb_y (x=3, y=2) composition

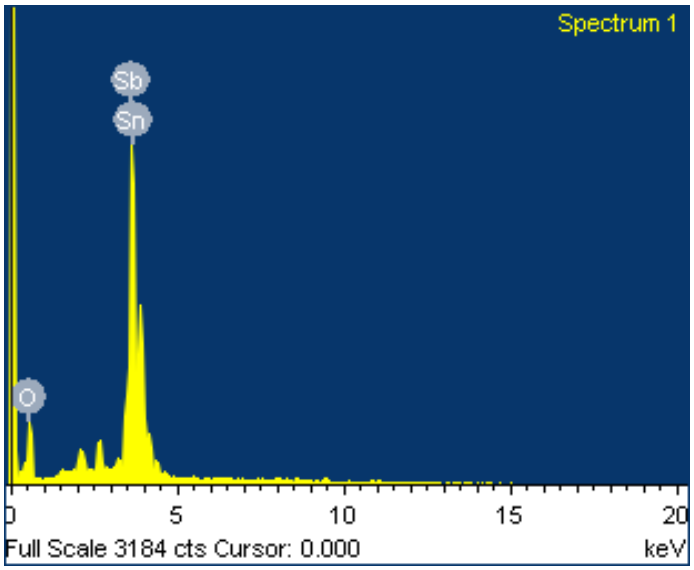

Figure 4.4 (d) EDX Image for Sn_xSb_y (x=3, y=4) composition

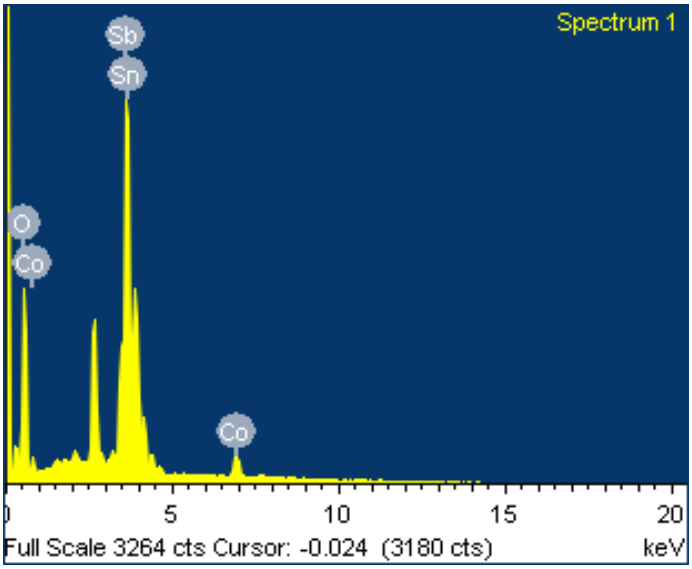

Figure 4.4 (e) EDX Image for Sn_xSb_y-Co (x=3, y=4) composition

Table 4.2 Compositional analysis for Sn_xSb_y and Sn_xSb_y-Co (x=2-3, y=2-4)

Sn_xSb_y	Atomic Weight %		
	Sn	Sb	Co
2:3	9.1156	90.884	-
2:3 (0.2)	0.64	94.85	4.51
3:2	0.9426	99.057	-
3:4	1.7357	98.2642	-
3:4 (0.5)	10	79.699	10.31

4.3 Optical Characterization

4.3.1 Fourier Transform Infrared Analysis (FTIR)

Figure 4.5 (a), (b), (c) and (d) shows the FTIR spectrum of Sn_xSb_y and Sn_xSb_y-Co (x=3, y=4) samples.

FTIR spectra of SnSb and SnSb: Co of nano particle recorded at room temperature in the wavelength range of 4000- 400 cm^{-1}. Since the spectrum was obtained using KBr pelletization process, OH stretching and vibration peak at 3514-3251 cm-1 is observed due to hygroscopicity. Few peaks are observed to change in

dimension from the undoped while adding Co to the crystalline structure. The peak at 1068 cm^{-1} has been diminished indicating the weakening of Sn to Sb bonding. Similarly the bonding which was weaker at 1572 cm^{-1} shows significant strengthening due to Co addition. A new peak at 1751 cm^{-1} arose indicating the Co-Sn or Co-Sb bond creation in the structure. Altogether, it is very clear that Co has well bonded itself in the crystal structure of rhombohedral structure. When looked in combination with the XRD analysis the rhombohedral structure is well preserved even Co entered and bound itself in the structure.

Comparing the FTIR spectra for the ratios of 3:2 and 3:4, the absorption peaks between 400- 800cm^{-1} shows drastic difference. Looking into the chemical composition is very much less than Sb in both the samples however Sn is prominently large in 3:4 sample. Hence the suppression of these peak in 3:4 samples Figure 4.5 (b) indicates fewer Sn-Sn bonding with respect to 3:2 sample Figure 4.5 (a). The overall broadening of these peaks when Co is substituted Figure 4.5 (c) and (d) indicates that pronounced bondage between Sn-Co due to substitution of Co in Sn sites to occur.

The absorption at 1600 cm^{-1} is in the descending order 3:4 (0.2) >3:4 (0.5) > 3:2 > 3:4. This variation could be well correlated with the SnSb (101) plane. Antimony form hexagonal structure with six atoms per cell under normal conditions. In SnSb structure as the JCPDS data (# 330118) suits well for the rhombohedral structure with a space group of $R\bar{3}m$ which contains two antimony atoms (i.e., all the other four are Sn atoms). Then (101) plane contains $(1/3)^{rd}$ of an atom and rest are Sn atoms. Any change in (101) plane need to be substitution or skew of Sn atom only [5].

Sn_3Sb_2

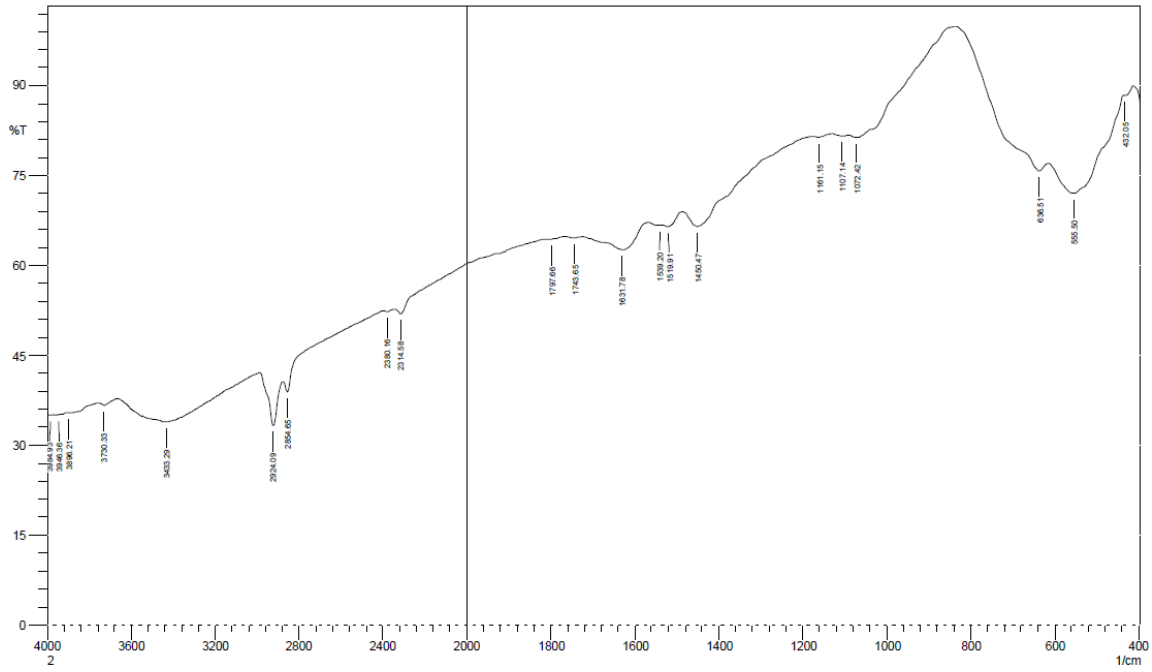

Figure 4.5(a) FTIR Spectra Sn_xSb_y (x=3, y=2)

Sn_3Sb_4

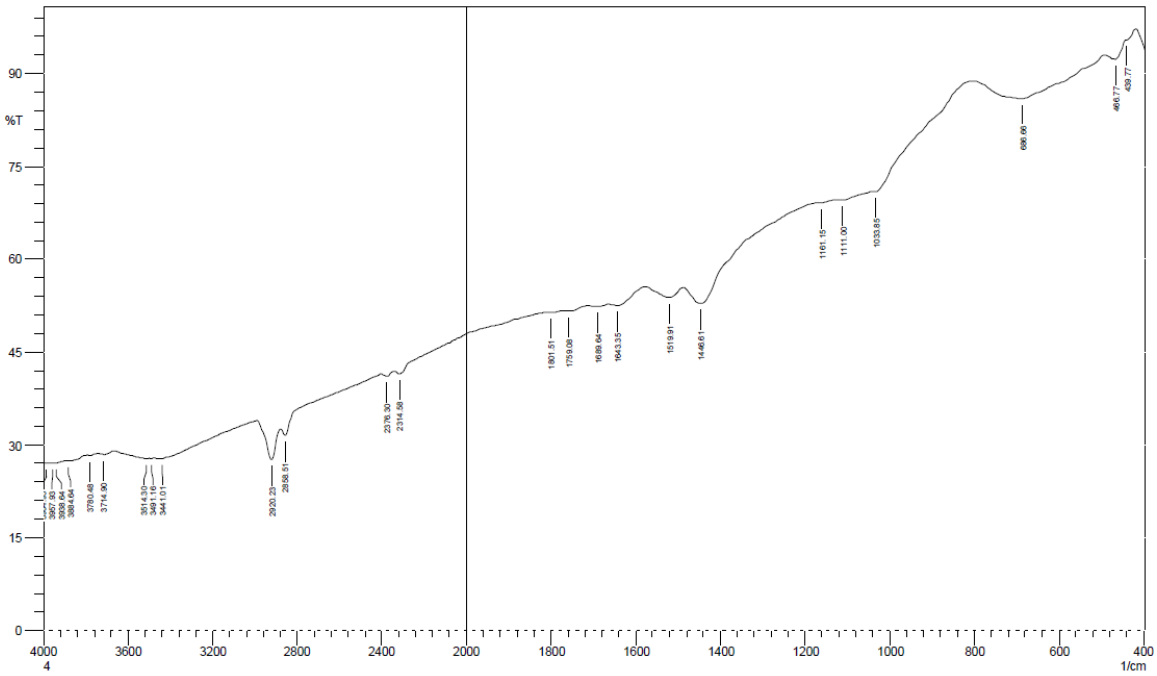

Figure 4.5(b) FTIR Spectra Sn_xSb_y (x=3, y=4)

Sn_3Sb_4-Co (0.2)

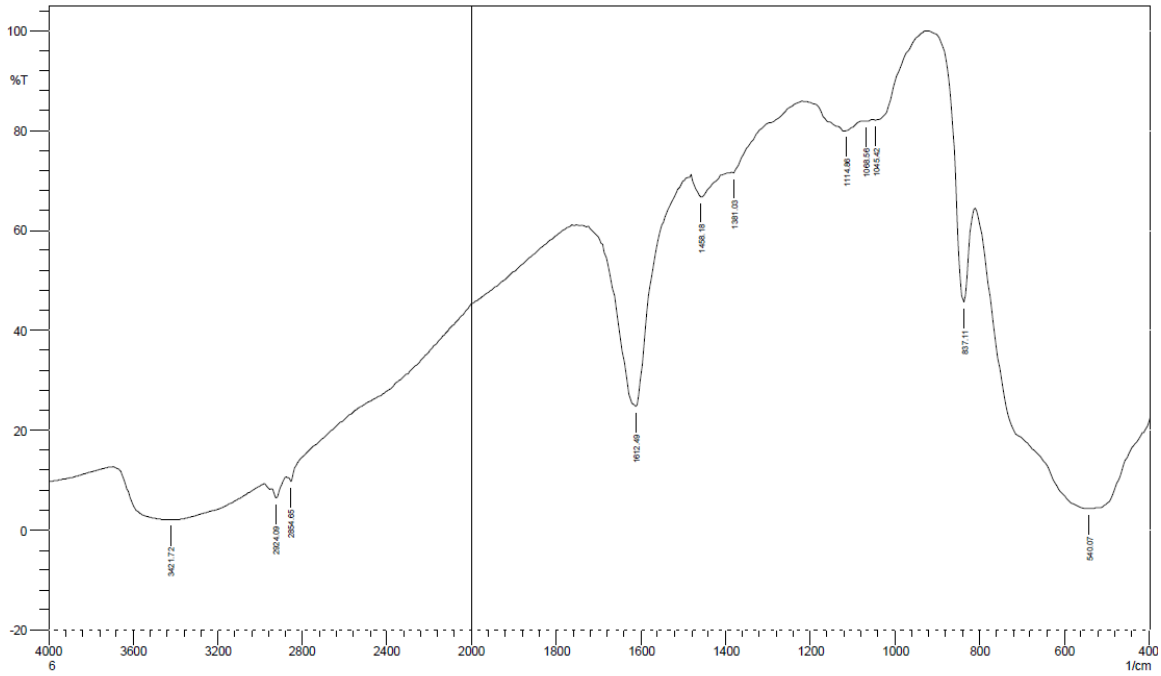

Figure 4.5(c) FTIR Spectra Sn_xSb_y-Co(x=3, y=4) (0.2)

Sn_3Sb_4- Co (0.5)

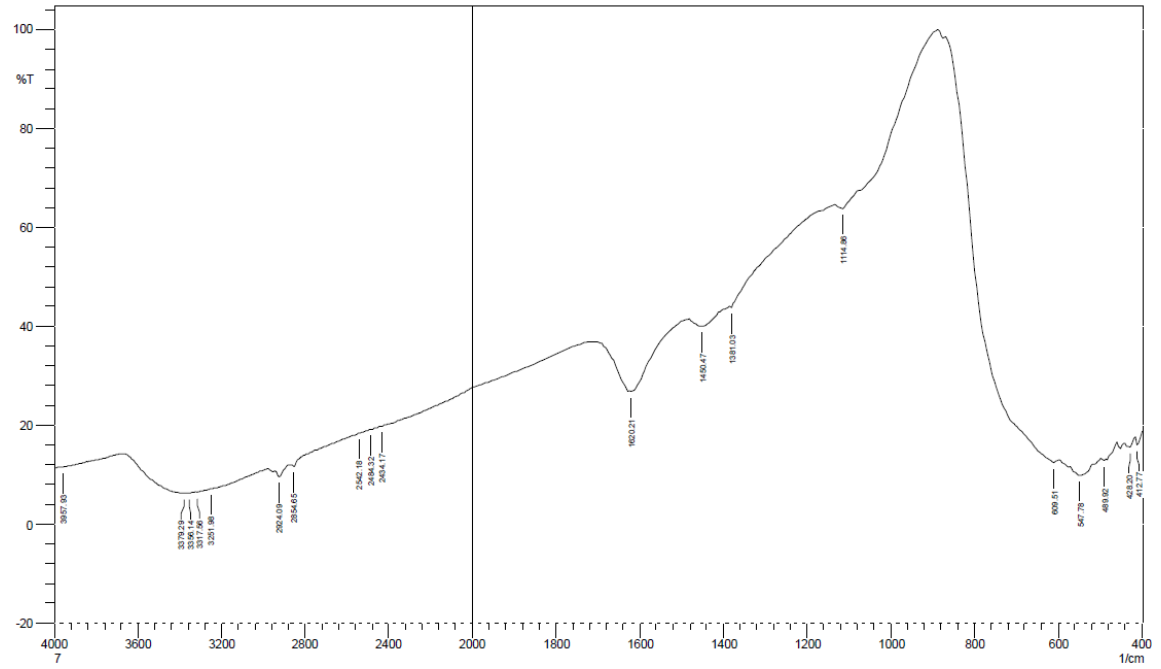

Figure 4.5(d) FTIR Spectra Sn_xSb_y-Co(x=3, y=4) (0.5)

4.4 References

1. Kuok Hau Seng, Zai Ping Guo, Zhi Xin Chen, and Hua Kun Liu; SnSb/Graphene Composite as Anode Materials for Lithium Ion Batteries; Advanced Science Letters; 4; 18–23; 2011.
2. V. P. Vasilev; A Complex Study of the Phase Diagram of the Sn–Sb System; Russian Journal of Physical Chemistry; 79(1); 20–28; 2005.
3. H.K.Liu; Journal of alloys and compounds; 400; 234; 2005.
4. Yuanwen Zou, Zhongbing Huang, Yan Wang, Xiaoming Liao, Guangfu Yin, Jianwen Gu; Synthesis and cellular compatibility of Co-doped ZnO particles in silk-fibroin peptides; Colloids and Surfaces B: Biointerfaces; 102; 29– 36; 2013.
5. T. Tabuchi, N. Hochgatterer, Z. Ogumi and M. Winter, Ternary Sn-Sb–Co alloy film as new negative electrode for lithium-ion cells, Journal of Power Sources, 188(2), 552–557, 2009.

CHAPTER-V
SUMMARY AND CONCLUSION

5.1 Conclusion

Sn_xSb_y alloys with Sn to Sb ratios 2:3, 3:2, 3:4 were prepared and cobalt is substituted in all these composition. The composition 2:3, 2:3 Co(0.2), 3:2, 3:4 are possessing single phase and rhombohedral structure. But 3:2 has to be critically analyzed for phase formation since the trials left single and mixed phase intermittently. The Energy Dispersive X-ray analysis (EDX) has been conducted and the molecular formula has been obtained. SEM analysis shows agglomerations and grain sizes varying from 3-20 μm. Also the lattice strain is observed due to the addition of cobalt through Fourier Transform Infrared spectroscopy (FTIR) studies. Hence it is concluded that single phase formation which was not possible by solid state reaction method is possible through co-precipitation method but need to be critically analyzed for optical conditions cobalt substitution is likely to occupy the Sn sites and hence the crystallinity is also brought down.